A&A 474, 941–950 (2007)
DOI: 10.1051/0004-6361:20078260

Astronomy & Astrophysics

Quantitative optical and near-infrared spectroscopy of H_2 towards HH91A[★,★★]

R. Gredel

Max-Planck Institute for Astronomy, Königstuhl 17, 69117 Heidelberg, Germany
e-mail: `gredel@mpia.de`

Received 12 July 2007 / Accepted 31 August 2007

ABSTRACT

Aims. Optical and near-infrared spectroscopy of molecular hydrogen in interstellar shocks provide a very powerful probe of the physical conditions that prevail in interstellar shocks.

Methods. Integral-field spectroscopy of H_2 in the optical wavelength region and complementary long-slit near-infrared spectroscopy towards HH91A are used to characterize the ro-vibrational population distribution among H_2 levels with excitation energies up to 30 000 cm^{-1}.

Results. The detection of some 200 ro-vibrational lines of molecular hydrogen ranging between 7700 Å and 2.3 μm is reported. Emission lines which arise from vibrational levels up to $v' = 8$ are detected. The H_2 emission arises from thermally excited gas where the bulk of the material is at a temperature of 2750 K and where 1% is at 6000 K. The total column density of shocked molecular hydrogen is $N(\mathrm{H_2}) = 10^{18}\ \mathrm{cm}^{-2}$. Non-thermal excitation scenarios such as UV fluorescence do not contribute to the H_2 excitation observed towards HH91A.

Conclusions. The emission of molecular hydrogen towards HH91A is explained in terms of a slow J-shock that propagates into a low-density medium, that has been swept up by previous episodes of outflows that have occurred in the evolved HH90/91 complex.

Key words. ISM: molecules – ISM: Herbig-Haro objects – ISM: jets and outflows

1. Introduction

The study of molecular hydrogen emission lines in star-forming regions provides a powerful tool to gain insight into the physical processes which occur during the early stages of star formation. Outflows from young stellar objects drive powerful shock waves into the interstellar medium. The heating associated with the shocks can give rise to the excitation and dissociation of H_2. For low-mass protostars, the total H_2 luminosities are proportional to the accretion rates during the early phases of the protostellar evolution, and evidence exists that the proportionality also extends to the high-mass stellar regime (Froebrich et al. 2003; Davis et al. 2004; Caratti o Garatti et al. 2006; Gredel 2006). These findings support a scenario where high-mass star formation proceeds via accretion as well, but at significantly larger accretion rates compared to their low-mass counterparts (e.g. McKee & Tan 2003; Yorke & Sonnenhalter 2002). The shock waves that lead to H_2 emission are either continuous (C-shock) or jump type (J-shock), depending on the physical conditions in the pre-shock gas, such as the magnetic field strength and the degree of ionization. The physical parameters and the H_2 luminosities depend on the evolutionary state of the driving source. For instance, jets from Class 0 sources travel in the high density gas from which the protostars are forming, and strong H_2 emission from C-type shocks is expected. Jets from older protostars propagate into a medium at lower density, since the mass lost during the early phase of the protostellar evolution has already swept up much of the ambient gas; these conditions favor dissociative J-type shocks (Caratti o Garatti et al. 2006). The C-type shocks produce a large column of warm gas in the $v' = 0$ levels of H_2, while the J-type shocks produce large columns of hot gas of several 1000 K in the higher vibrational levels (Cabrit et al. 2004; Smith et al. 2007, and references therein).

Comprehensive near-infrared spectroscopy of molecular hydrogen emission in Herbig-Haro (HH) objects covering the *J*-, *H*-, and *K*s-bands has been used to probe the physical conditions in molecular outflows from protostars (e.g. Caratti o Garatti et al. 2006, and references therein). The H_2 emission in Herbig-Haro objects is, in general, dominated by thermal emission which arises from rotational levels in $v' = 1$–5. In general, the observed H_2 emission is explained by J-type shocks (Smith 1994; Gredel 1994, 1996; McCoey et al. 2004; Nisini et al. 2002, among others), yet it has been noted that the population distribution among ro-vibrational levels in $v' = 1$–5 is not the best discriminator to unambiguously infer the type of shock that is involved (Flower et al. 2003). Using emission from pure rotational lines in the (0, 0) band of H_2, Giannini et al. (2006) convincingly demonstrated that the emission towards HH54 arises from a steady-state J-shock.

In the following sections, a quantitative study of the molecular hydrogen emission in HH91A is presented. The novel aspect of the present study is given by the study of H_2 emission lines in the optical wavelength region between 7700−8700 Å, and the study of relatively faint emission lines that arise from very high-excitation ro-vibrational levels in the near-infrared.

[★] Based on observations collected at the Centro Astronomico Hispano Aleman (CAHA) Calar Alto, operated jointly by the Max-Planck Institute for Astronomy and the Instituto de Astrofisica de Andalucia (CSIC). Based on observations collected at the European Southern Observatory, La Silla, Chile.

[★★] Tables 2–4 and Figs. 10–16 are only available in electronic form at `http://www.aanda.org`

HH91A is part of the HH90/91 complex of Herbig-Haro (HH) objects, which is located in the L1630 cloud. A comprehensive optical/infrared/millimeter study has been performed by Gredel et al. (1992). Complementary near-infrared observations were presented by Davis et al. (1994). These studies report widespread and diffuse emission of molecular hydrogen which extends over several square arcmin. A number of very bright H_2 knots, such as HH91A, are superimposed. The bulk of the H_2 emission from HH91A arises from hot gas at a temperature of 2750 K (Gredel et al. 1992). Deep near-infrared imaging by Moneti & Reipurth (1995) did not detect the energy source that drives the HH90/91 outflow. HH90/91 is thought to be a fairly evolved Herbig-Haro object (Gredel et al. 1992).

Because the H_2 emission towards HH91A is very bright indeed, HH91A affords the possibility of studying emission from very high-excitation levels of H_2 that arise in the optical and near-infrared wavelength regions. The population density of these levels provides a very sensitive discriminator among the various physical processes that contribute to the excitation of H_2 in shocks. The optical spectra of HH91A obtained with the integral field spectrograph PMAS at the Calar Alto 3.5 m telescope are described in Sect. 2, together with complementary near-infrared spectra obtained with SOFI at the ESO/La Silla New Technology Telescope. The results are summarized in Sect. 3, which also contains a description of a theoretical model of H_2, which is compared with the observations. We conclude with a discussion of the significance of non-thermal excitation scenarios of the H_2 emission towards HH91A in Sect. 4.

2. Observations and reduction

Optical spectroscopy of HH91A was carried out during the nights of Feb. 15 and 16, 2004, using the Potsdam Multi-Aperture Spectrophotometer PMAS at the Calar Alto 3.5 m telescope (Roth et al. 2005). PMAS is an integral field instrument and was used in its standard configuration with a 16 × 16 lenslet array of $8'' \times 8''$ on the sky. The R1200 reflective grating provided a spectral resolution of approximately $R = \lambda/\Delta\lambda = 10\,000$. The grating was used at encoder settings of 49° and 46°, which resulted in spectral coverage of 7690–8270 Å and 8400–8980 Å, respectively. Sky-subtraction was achieved using the nod-and-shuffle technique (Roth et al. 2004), where the charge-shuffle mode of the CCDs is used to perform beam-switching between HH91A and a sky position during ongoing integrations. This mode results in a very high degree in the accuracy of the sky subtraction. Atmospheric transmission was corrected via the observation of various telluric standard stars. The data were obtained during non-photometric observing conditions that did not allow us to derive a flux calibration. However, a number of H_2 emission lines in the 7700–8700 Å optical spectra arise from the same upper ro-vibrational levels as emission lines in the near-infrared wavelength region. Examples are the (4, 1) S(3) line near 8500 Å and the (4, 2) S(3) and (4, 2) Q(5) lines in the J-band that arise from $v' = 4$, $J' = 5$, or the (3, 0) S(3), (3, 0) Q(5) in the optical and the (3, 1) S(3) and (3, 1) Q(5) lines, which arise from $v' = 3$, $J' = 5$. The near-infrared observations were obtained during photometric conditions, and the H_2 population densities inferred from the near-infrared observations were used to obtain a relative flux calibration for the optical spectrum. We ignore reddening towards HH91A (Gredel et al. 1992). The PMAS observations afford the possibility of studying spatial variations in line ratios across the H_2 line emitting regions. The H_2 emission detected in the optical wavelength regime is very faint indeed. The spectra in a PMAS pixel (0.25 square arcseconds) have a signal to noise ratio that is too low to derive meaningful conclusions. We sum all spectra over the central $5''$ emission region, therefore the PMAS observations cannot be used to study changes in the H_2 excitation across HH91A.

The near-infrared spectra cover the J, H, and Ks-band atmospheric windows and were obtained during the nights of Dec. 20 and 21, 2003, using SOFI at the La Silla New Technology Telescope NTT. The reduction of the data and the flux calibration were performed according to methods described elsewhere (e.g. Gredel 2006). The observations were carried out during photometric conditions and thus allow us to infer total column densities in the various ro-vibrational levels of H_2 (see Gredel 2006, for details). The spectra were obtained using a slit width of $0\farcs6$. The blue grism GB in order 1 and the HR grism in orders 2 and 1 were used, which provide spectral resolutions of $R = 600$, 1560, and 1800 in the J-, H-, and Ks-bands, respectively. The one-dimensional spectra were extracted using a 20-pixel extraction window along the slit ($5\farcs8$), which corresponds to an "aperture" of 3.6 square arcseconds or a solid angle of $\Omega = 9 \times 10^{-11}$ sr^{-1}.

3. Results

3.1. Optical spectroscopy using PMAS

The optical spectra obtained towards HH91A are shown in Figs. 1 and 2. Emission from the (3, 0) S(1)–S(14) lines is detected long-ward of the (3, 0) S-branch band head marked by the (3, 0) S(8) line at 7781 Å (Fig. 1). The (3, 0) Q(1)–Q(6) lines are also detected, together with several lines in the (4, 1) S-branch (Fig. 2). The (8, 4) S(9) line near 8496 Å is clearly detected. A wavelet analysis of the optical spectra confirms the marginal detection of the (7, 3) S(11) line at 7978 Å, and of the (8, 4) S(11) lines near 8763 Å. The signal to noise ratio in the latter two lines is very low indeed, and as a standalone result, the claim of the detection of the latter three emission lines in our spectra may be disputed. The red lines in Figs. 1 and 2 reproduce the expected fluxes in the (7, 3) S(11) and (8, 4) S(9) and S(11) lines from a model which is presented in detail below. The model is based on the analysis of the full set of some 200 observed H_2 emission lines towards HH91A, and substantiates the result from the wavelet analysis, which indicates that emission from the (7, 3) and (8, 4) bands towards HH91A is detected.

3.2. Near-infrared spectroscopy using SOFI

The near-infrared spectra obtained with SOFI are reproduced in Figs. 3–7. The J-band spectra shown in Figs. 3 and 4 are dominated by emission from the (2, 0) S-branch (band-head near 1.055 μm), the (3, 1) S-branch (band-head near 1.118 μm), the (4, 2) S-branch (band-head near 1.185 μm), and the (5, 3) S-branch (band-head near 1.282 μm). Strong emission lines from the (2, 0), (3, 1), and (4, 2) Q-branch are also detected. In addition, various emission lines from the (6, 3) S-branch band are detected long-ward of its band-head near 9506 Å, and from the (7, 4) S-branch (band-head 10 028 Å, cf. Fig. 3). The inferred population densities in the ro-vibrational levels of $v' = 6$ imply that emission in the (6, 4) band occur at flux levels above the noise of the spectra presented here. The (6, 4) Q(1)–Q(9) lines are clearly detected (see below). The expected emission lines in (6, 4) S-branch, up to the band-head marked by the (6, 4) S(8) line, near 13 840 Å, is reproduced in Fig. 4 by the red line. The (6, 4) S-branch is located in a region of poor atmospheric transmission between 1.35−1.5 μm, where the fluxes of the measured

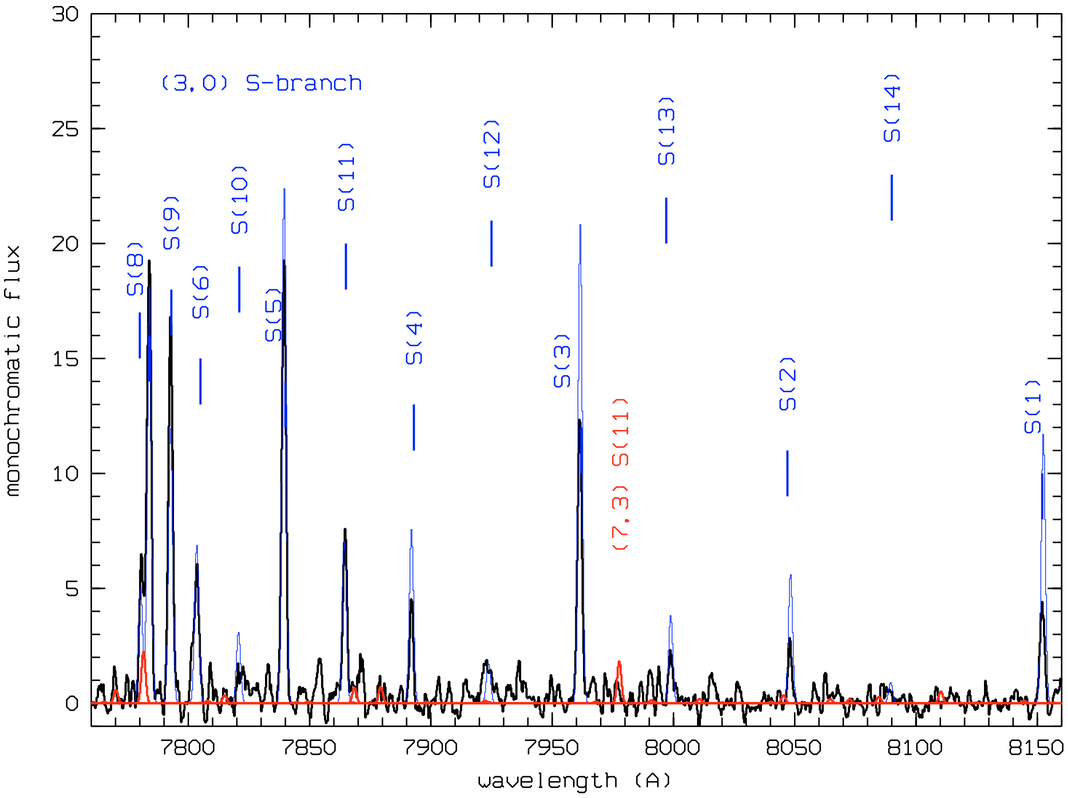

Fig. 1. Observed spectrum towards HH91A obtained with PMAS, with monochromatic fluxes plotted versus wavelength (in Å). The positions of the (3, 0) S(1)–S(14) lines are indicated. The (7, 3) S(11) line near 7978 Å is marginally detected. Model spectra with emission from vibrational levels $v' = 3$ and 7 are color-coded in blue and red, respectively (cf. Sect. 4). The emission near 8727 Å arises from atomic carbon.

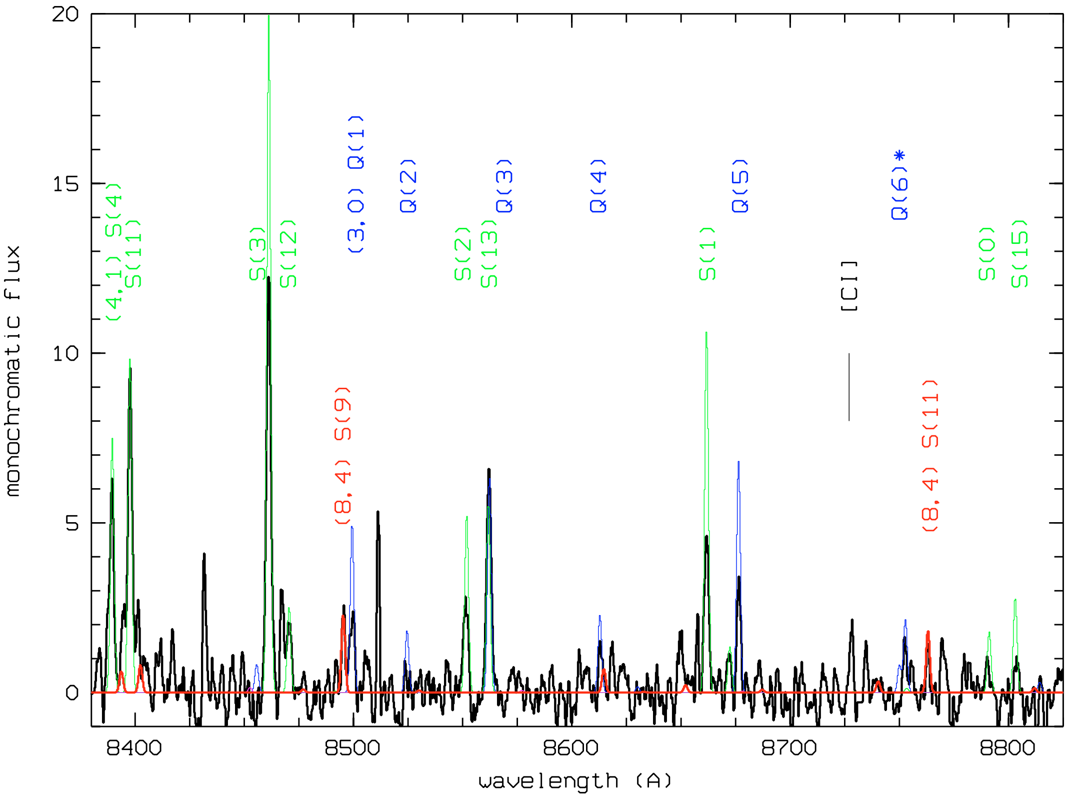

Fig. 2. Observed spectrum towards HH91A obtained with PMAS, with monochromatic fluxes (in relative units) plotted versus wavelength (in Å). The position of various emission lines in the (3, 0) and (4, 1) bands is indicated. The (8, 4) S(9) and (8, 4) S(11) lines near 8500 Å and 8685 Å, respectively, are marginally detected. The emission lines color-coded in blue, green, and red correspond to model spectra with emission from vibrational levels $v' = 3$, 4, and 8, respectively (cf. Sect. 4).

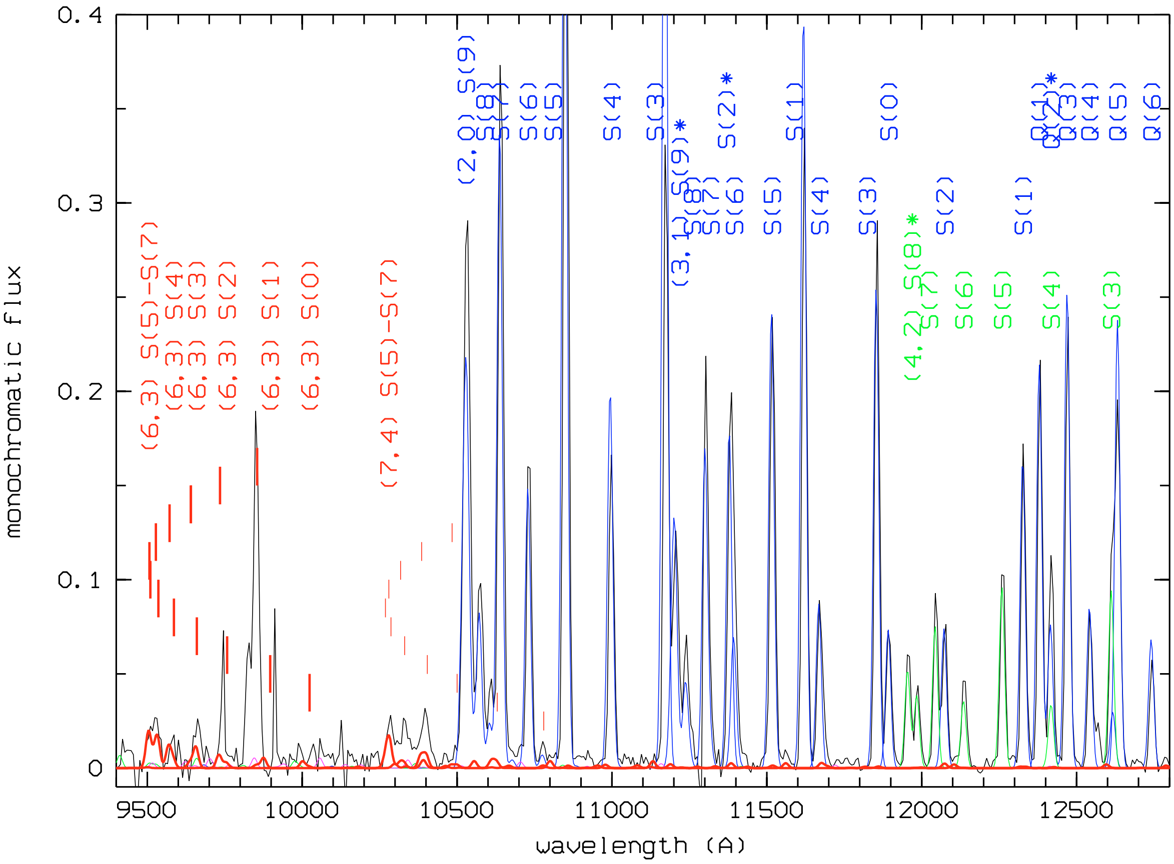

Fig. 3. *J*-band spectrum towards HH91A obtained with SOFI. Monochromatic fluxes are plotted in units of 10^{-17} W m^{-2} μm^{-1} vs. wavelength in units of Å. The spectrum is dominated by strong emission lines which arise from the (2, 0), (3, 1), and (4, 2) S-branches. Faint emission from various lines in the (6, 3) and (7, 4) *S*-bands is detected. The positions of the various lines in the (6, 3) S-branch between 9500–10 000 Å are indicated. The positions of several lines converging to the band-head of the (7, 4) S-branch between 10 030–10 050 Å are also indicated. The emission near 9825 Å and 9851 Å arises from the $^1D_2$–$^3P_1$ and $^1D_2$–$^3P_2$ transition of [CI]. The theoretical H_2 emission spectrum is reproduced in color, with emission from $v' = 2$ and 3 in blue, from $v' = 4$ in green, and from $v' = 6$ and 7 in red.

emission lines are highly uncertain. The modeled emission in the (6, 4) S-branch is consistent with the observations. The emission feature near 9825–9851 Å corresponds to emission from atomic carbon (cf. Sect. 4). Emission from [FeII], which is generally observed in HH-objects, is absent.

The *H*-band spectra towards HH91A are shown in Figs. 5 and 6. The *H*-band spectrum is dominated by strong emission from the (1, 0) S-branch (band-head marked by (1, 0) S(14) near 16 296 Å) and relatively strong emission from the (3, 1) O(5)–O(7), (4, 2) Q(11)–Q(13). In addition, emission from (6, 4) Q(1)–Q(9) is detected. The bold red line reproduced in Figs. 5 and 6 corresponds to the theoretical emission from a model presented below.

Finally, the *K*s-band spectrum is shown in Fig. 7. The emission is dominated by the very strong (1, 0) S(0)–S(2) lines and the (2, 1) S(1)–S(4) lines. Emission from (3, 2) S(2)–S(5) and from (4, 3) S(4) is also detected. The strong H_2 lines, such as the (1, 0) S(7) and the (1, 0) S(1) lines, show pronounced line wings. These wings have no astrophysical significance and arise from an instrumental defect of SOFI, which is evident since these lines do not show wings in the spectra taken previously with IRSPEC (Gredel et al. 1992).

The spectra shown in Figs. 1–7 contain some 200 emission lines of molecular hydrogen. The inferred fluxes *F* of the various lines are given in Col. 3 of Tables 1 and 2, with flux uncertainties in parenthesis. The optical spectra have limiting line fluxes of about 0.5×10^{-19} W m^{-2}, as judged from noise in the flux-scaled spectra (see above). Limiting fluxes are about 10^{-19} W m^{-2} in the spectra taken with grism GB, 0.5×10^{-19} W m^{-2} in the *H*-band, and 10^{-19} W m^{-2} in the *K*s-band taken with grism HR. For the stronger lines, flux uncertainties introduced by the calibration of the atmospheric transmission are estimated to be of the order of 10–20% of the total line flux. Fluxes derived from emission lines that occur in spectral regions that are dominated by narrow, telluric absorption lines, such as the 13 500–15 000 Å region, are uncertain by larger amounts. Columns 1, 2, and 4 contain the line identification, the vacuum wavelength λ, and the inferred column density $N(v'J')$ of the corresponding upper ro-vibrational level $v'J'$, respectively. Numbers in parenthesis in Col. 4 of Tables 1 and 2 are uncertainties in column densities.

Because of the relatively low spectral resolution provided by SOFI, many of the features detected in the *J*-, *H*-, and *K*s-bands are blends of two or more emission lines of H_2. In cases of line blends, no effort was made to de-convolve the lines or to assign fractional flux values to the individual components. Rather, the full line flux was assigned to each one of the possible ro-vibrational lines that occur at the given wavelength. Examples are the (4, 2) S(9) + S(10) blend near 1.196 μm, the (2, 0) Q(2) + (4,2) S(4) blend near 1.242 μm, the (4, 2) S(2) + (5,3)S(10) blend near 1.284 μm, and the (2, 0) Q(7) + (5,3)S(7) blend near 1.288 μm. The entries in Table 2 are thus to be read with care; in cases when line blends occur, the listed H_2 column densities are

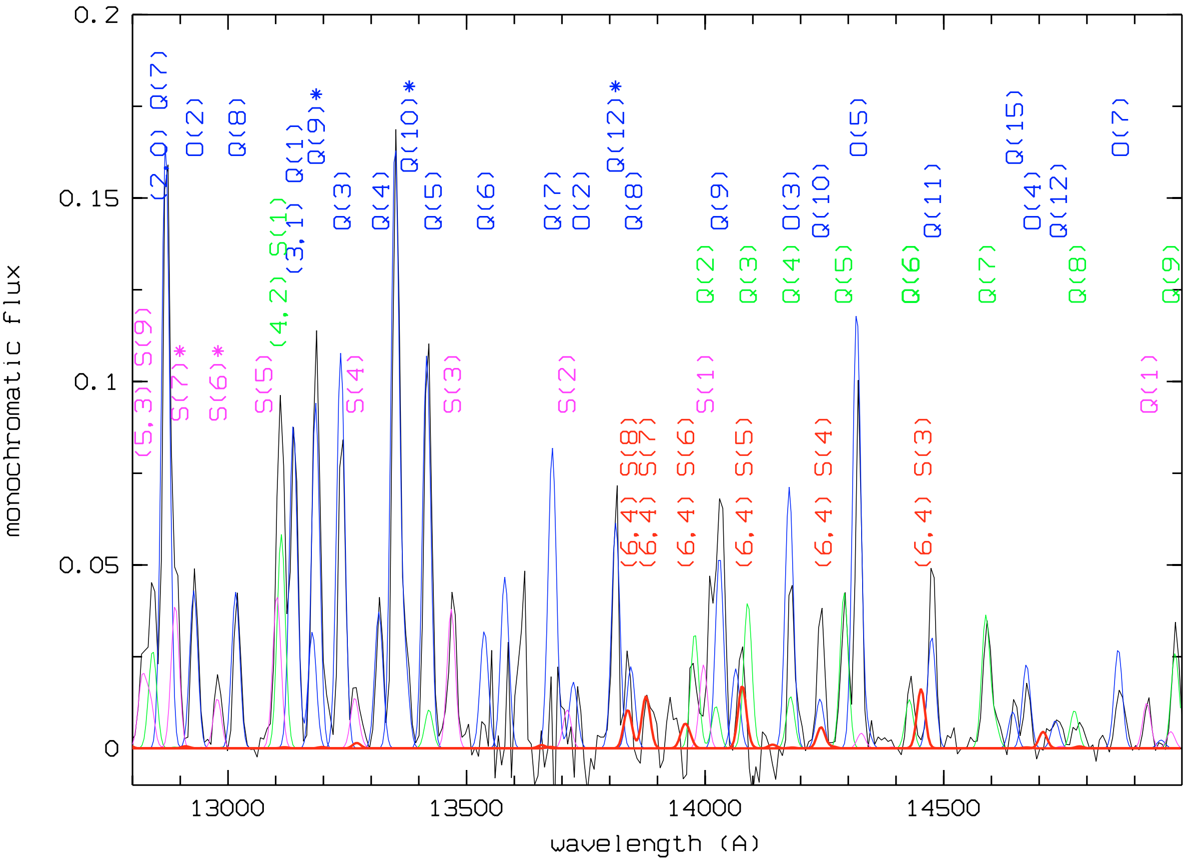

Fig. 4. J-band spectrum towards HH91A, with monochromatic fluxes in units of 10^{-17} W m^{-2} μm^{-1} vs. wavelength in units of Å. The strong emission lines which arise from the (2, 0), (3, 1), (4, 2), and (5, 3) bands are identified. The expected position and strength of modeled emission from the (6, 4) S(3)–S(8) lines is also indicated (cf. Sect. 4). The theoretical H_2 emission spectrum is reproduced in color, see Fig. 3 for details.

too large. Unresolved line blends are identified by an asterisk in Figs. 3–7 and in Table 2.

The H_2 column densities listed in Tables 1 and 2 are nevertheless used to construct the H_2 excitation diagram with values of $\ln(N(v'J')/g)$ plotted versus excitation energy $E(v'J')$ (see e.g. Gredel 2006, for details). The diagram is reproduced in Fig. 8. The occurrence of line blends introduces some scatter in the excitation diagram. The scatter has no physical origin, nor is it introduced by non-thermal excitation scenarios. This statement is justified in detail in Sect. 4 below. We proceed to derive the ro-vibrational excitation temperature of the $v'J'$ levels in the following iterative way. The population densities in the H_2 levels up to an excitation energy of approximately 10^4 cm^{-1} is consistent with an excitation temperature of 2750 K, which is the temperature derived by Gredel et al. (1992) from their IRSPEC spectra, which were obtained at a higher spectral resolution than the spectra presented here. The population densities among the ro-vibrational levels above excitation energies of 10^4 cm^{-1} deviate from the population densities expected for a thermalized distribution at 2750 K. The deviation causes a *curvature* in the excitation diagram and indicates that a fraction of 1% of the gas is at the very high temperature of 6000 K. This statement assumes that all the levels up to excitation energies of about 30 000 cm^{-1}, or about 40 000 K, are thermalized. Higher gas-kinetic temperatures are possible in principle, if it is assumed that the levels are sub-thermally excited. The curvature in the H_2 excitation diagram is not very pronounced and is only established through the observation of high-excitation emission lines with excitation energies above 15 000 cm^{-1}. This is the reason why the curvature went unnoticed in the earlier work of Gredel et al. (1992). The relatively low degree of temperature stratification in HH91A, combined with the absence of emission from [FeII], supports the general finding of Caratti o Garatti et al. (2006) who concluded that a significant temperature stratification in the H_2 emitting gas is generally observed in HH-objects that show [FeII] emission as well.

In order to judge whether the above conclusions are fully consistent with the observed optical and near-infrared spectra, we have modeled the spectrum expected from a two-component gas mixture at a temperature of 2750 K, and where a fraction of 1% of the gas is at a temperature of 6000 K. We have used the models of Gredel & Dalgarno (1995) to calculate the theoretical H_2 emission spectrum. From the entry rates into the ro-vibrational levels $v'J'$ of the electronic ground state of H_2, a spectrum (Voigt profiles) is calculated as a function of parameters such as the total H_2 column density, the reddening E_{B-V}, the desired spectral resolution $R = \lambda/\Delta\lambda$, etc. We ignore reddening towards HH91A (cf. Gredel et al. 1992) and calculate the expected emission spectra for the various spectral resolutions in the PMAS and SOFI spectra. Apart from the relative flux calibration of the PMAS spectra as discussed above, the only scaling that we use is introduced by a forced match of the predicted and calculated flux in the (1, 0) S(1) line. For a gas mixture of warm molecular gas at 2750 K plus a fraction of 1% at 6000 K, the model calculation produces a total H_2 flux of $F_{\rm tot}(H_2) = \Sigma_{v'J'v''J''} F(v'J'v''J'') = 19.8 \times F(1301)$, where $F(1301)$ is the flux in the (1, 0) S(1) line and where the summation is carried out over all possible emission lines of H_2. The

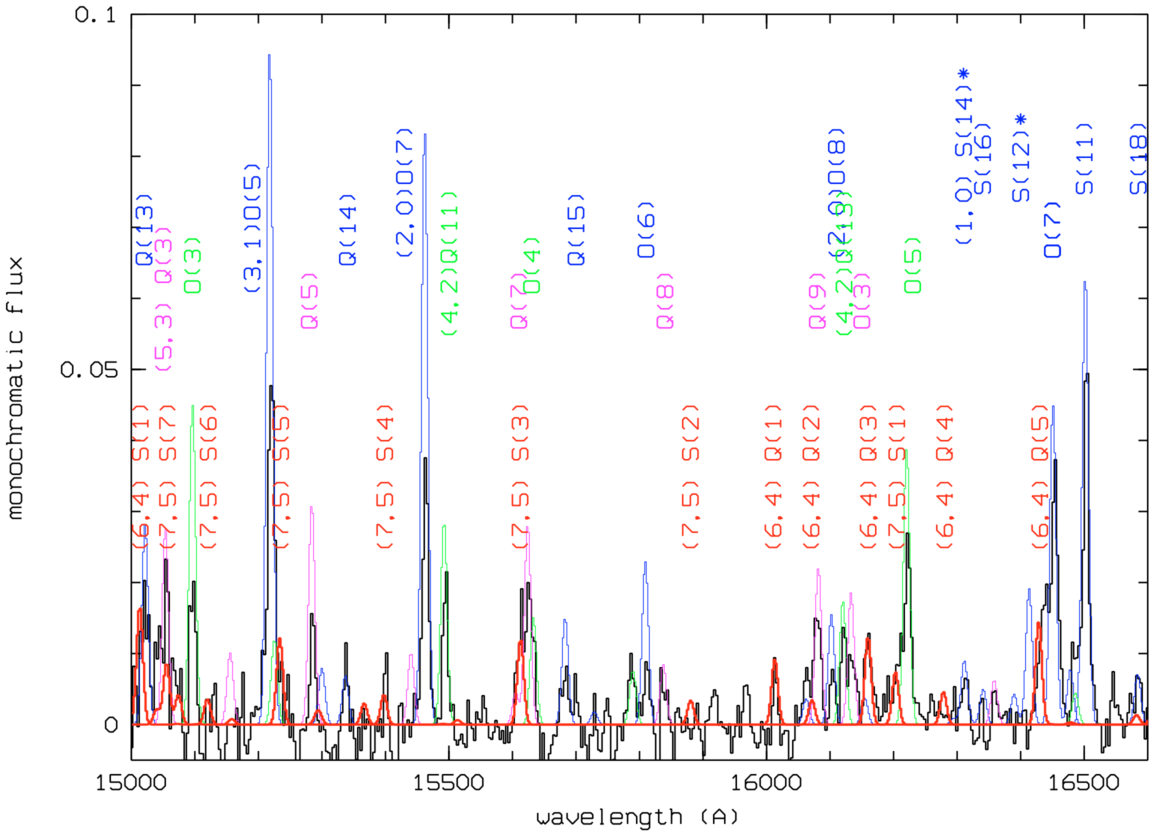

Fig. 5. *H*-band spectrum towards HH91A, with monochromatic fluxes in units of 10^{-17} W m^{-2} μm^{-1} vs. wavelength in units of Å. The emission lines reproduced in color correspond to a model calculation that is presented in Sect. 4. Emission from $v' = 1$, 2, and 3 in blue, $v' = 4$ in green, $v' = 5$ in magenta, and $v' = 6$ and 7 in red. It is noted that emission from [FeII] $a^4D_{7/2} - a^4F_{9/2}$ near 16 440 Å is absent.

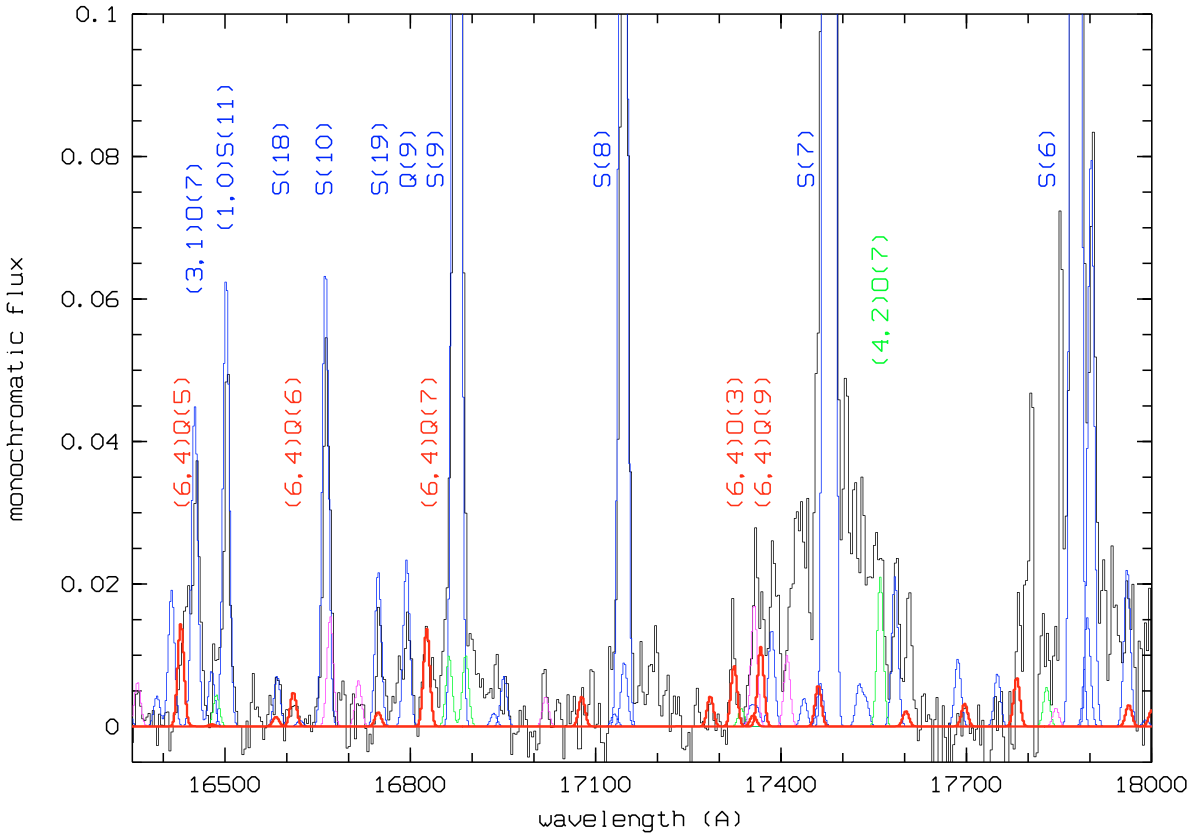

Fig. 6. *H*-band spectrum towards HH91A, see caption of Fig. 5 for details.

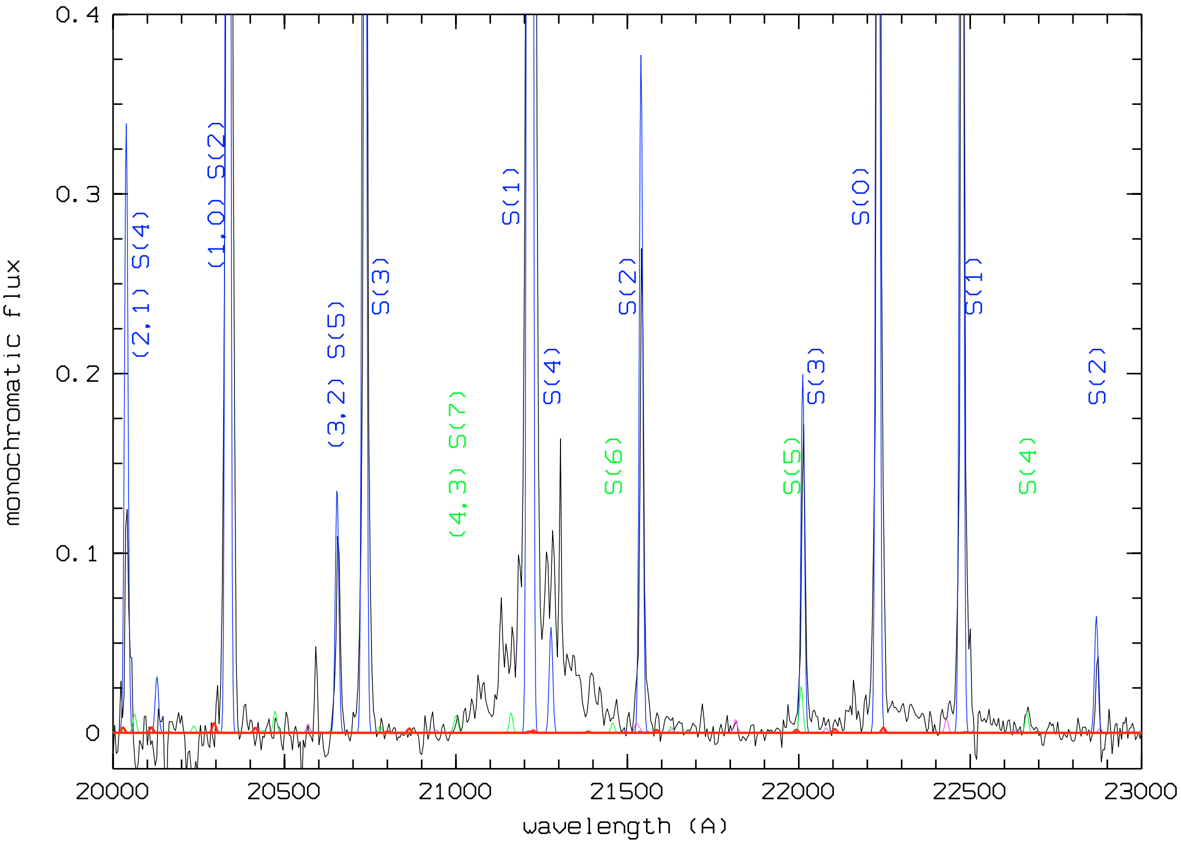

Fig. 7. *K*s-band spectrum towards HH91A obtained with SOFI, see caption of Fig. 5 for details. The wings in the (1, 0) S(1) line arise from an instrumental defect of SOFI and have no astrophysical significance.

total H_2 population density, for the two-component gas mixture adopted here, is $N_{\rm tot}(H_2) = \Sigma_{v'J'} N(v'J') = 45.7 \times N(1,3)$, or $N_{\rm tot}(H_2) = 1.26 \times 10^{18}$ cm^{-2}. The scaling factors (19.8 and 45.7 in the present case) are strongly dependent on the temperatures and column density ratios (cf. Gredel 1994).

The model calculations are reproduced by the colored lines in Figs. 1–7. In order to illustrate the contributions from the various vibrational levels of H_2, emission that arises from vibrational levels $v' \leq 3$ is color coded in blue, emission from $v' = 4$ in green, emission from $v' = 5$ in magenta, and emission from $v' \geq 6$ in red. The agreement of the modeled spectrum with the observations is excellent. In general, the line fluxes in the 200 or so observed emission lines of H_2 are reproduced within 20%. Relatively large deviations (factor of 2) between the model spectrum and the observations occur for the (3, 0) S(1) line near 8150 Å, for (4, 1) S(1) and (3, 0) Q(5) near 8670 Å, and for (3, 1) Q(7) near 1.37 μm, (3, 1) O(5) near 1.523 μm, and (2, 0) O(7) near 1.545 μm. The model also fails to reproduce the observed emission features near 1.03 μm but it does reproduce the (7, 5) S-branch in the *H*-band, which contains lines that arise from the same upper ro-vibrational levels as the lines near the (7, 4) S-branch band-head near 1.03 μm. This may indicate that emission other than from the (7, 4) S-branch occurs near 1.03 μm. The model spectrum demonstrates that fluxes of a few 10^{-20} W m^{-2} of individual ro-vibrational lines in the (6, 3), (6, 4), (7, 4), and (8, 4) bands are expected from a thermally excited gas towards HH91A. Among the various high-excitation lines, the band head of the (6, 3) S-branch near 9500 Å and the (6, 4) Q(1)–Q(9) lines in the *H*-band are perfectly reproduced by the model. Given that some of the discrepant lines occur in relatively poor atmospheric windows, and that the rest of the 200 or so observed lines are very well reproduced, and that fluxes among lines that arise from ro-vibrational levels that span excitation energies from 4000–30 000 cm^{-1} are accurately modeled, we ignore the discrepancies and conclude that the observed H_2 emission arises from thermal gas at 2750 K that contains a fraction of 1% at a temperature of 6000 K.

Tables 3 and 4 contain a full listing of our model results, and give expected H_2 emission lines that have integrated line fluxes above $F_{\rm tot} = 10^{-19}$ W cm^{-2} (Table 3) and fluxes ranging between $(0.5{-}1) \times 10^{-19}$ W m^{-2} (Table 4). The predicted thermal fluxes towards HH91A from the two gas components (bulk at 2750 K and 1% at 6000 K) are listed separately in Cols. 4 and 5, respectively. The tables contain the line identification, the wavelength in μm, and the energy of the upper ro-vibrational level in cm^{-1}, in Cols. 1–3, respectively. Total line fluxes are given in Col. 6. Figures 10–16 contain the residuals between the observed and the modeled H_2 line fluxes. As discussed earlier in Sect. 3, it can be seen that the overall agreement between the observed and the modeled spectra is excellent.

4. Discussion

Optical and near-infrared emission lines from molecular hydrogen that arise from very high-excitation ro-vibrational levels in the electronic ground state of H_2 are generally seen in sources where electronic states of H_2 are pumped in strong ultraviolet radiation fields, such as in NGC 2023 (McCartney et al. 1999). The absorption of ultraviolet radiation in the Lyman and Werner bands of H_2 (and the subsequent decay of the excited electronic states via dipole radiation) populates the ro-vibrational levels $v'J'$ of the electronic $X^1\Sigma_g^+$ ground state of

Table 1. Optical emission lines of H_2 detected with PMAS.

Line	Wavelength (Å)	Flux F (10^{-19} W m^{-2})	$N(v'J')$ (10^{14} cm^{-2})
(3, 0)S(8)	7781.	2.6(0.5)	1.3(0.3)
(3, 0)S(7)	7784.	8.1(0.8)	3.9(0.4)
(7, 3)S(9)	7782.	≤1	≤0.1
(3, 0)S(9)	7793.	6.9(0.7)	3.2(0.6)
(3, 0)S(6)	7804.	2.9(0.3)	1.6(0.3)
(3, 0)S(10)	7821.	≤0.4	≤0.2
(3, 0)S(5)	7840.	8.1(0.8)	4.9(1.0)
(3, 0)S(11)	7865.	3.0(0.3)	1.5(0.3)
(3, 0)S(4)	7892.	1.5(0.3)	1.1(0.3)
(3, 0)S(12)	7924.	≤0.4	≤0.2
(3, 0)S(3)	7962.	5.8(0.6)	4.9(1.0)
(7, 3)S(11)	7978.	≤0.4	≤0.1
(3, 0)S(13)	7999.	0.9(0.3)	0.6(0.2)
(3, 0)S(2)	8049.	1.0(0.3)	1.1(0.4)
(3, 0)S(14)	8090.	≤0.4	≤0.3
(3, 0)S(1)	8153.	2.3(0.3)	3.6(0.7)
(4, 1)S(4)	8390.	2.8(0.3)	0.7(0.1)
(4, 1)S(11)	8398.	4.1(0.4)	0.8(0.2)
(4, 1)S(3)	8462.	5.9(0.6)	1.6(0.3)
(4, 1)S(12)	8471.	1.0(0.3)	0.2(0.0)
(8, 4)S(9)	8496.	≤0.4	≤0.2
(3, 0)Q(1)	8500.	1.2(0.3)	2.8(0.7)
(3, 0)Q(2)	8525.	≤0.4	≤1.3
(4, 1)S(2)	8552.	1.4(0.3)	0.5(0.1)
(3, 0)Q(3)	8563.	3.3(0.3)	11.4(2.3)
(4, 1)S(13)	8562.	3.3(0.3)	0.8(0.2)
(4, 1)S(1)	8662.	2.5(0.3)	1.3(0.3)
(4, 1)S(14)	8673.	1.5(0.3)	0.4(0.1)
(3, 0)Q(5)	8677.	1.5(0.3)	5.4(1.1)
(3, 0)Q(4)	8613.	≤0.4	≤1.4
(3, 0)O(2)	8750.	≤0.6	≤1.2
(3, 0)Q(6)	8753.	≤0.6	≤2.3
(8, 4)S(11)	8763.	≤0.6	≤0.1
(4, 1)S(0)	8792.	≤0.6	≤0.5
(4, 1)S(15)	8803.	≤0.6	≤0.2

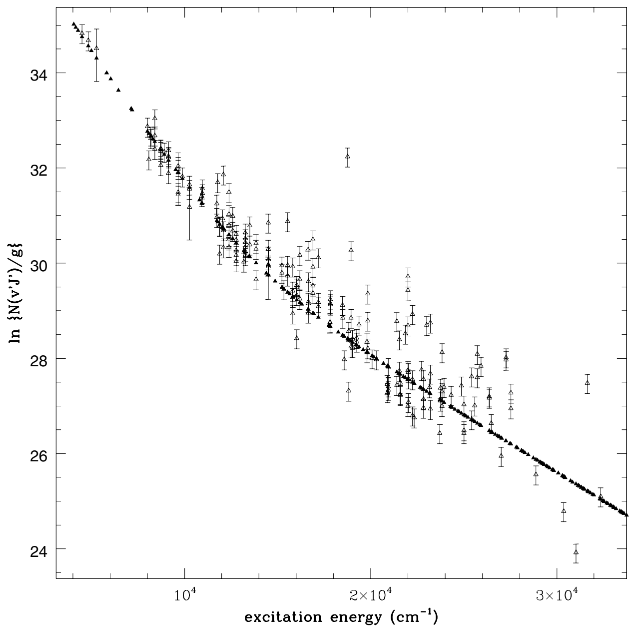

Fig. 8. H_2 excitation diagram with values of $\ln N(v'J')/g$ plotted versus excitation energy $E(v'J')$. Open triangles represent data points inferred from the column densities $N(v'J')$ listed in Tables 1 and 2. Filled triangles are obtained from a model calculation where the emission arises from a two-component gas model, where the bulk of the material has a total H_2 column density of 1.24×10^{18} cm^{-2} and is at a temperature of 2750 K, and where a fraction of 10^{16} cm^{-2} of H_2 is at a temperature of 6000 K.

H_2. The excited $v'J'$ levels cascade to lower ro-vibrational levels $v''J''$ via electric quadrupole (E2) radiation, and give rise to optical and near-infrared emission of H_2. In regions with strong X-ray radiation fields, electronic states of H_2 may also be collisionally excited by energetic secondary electrons produced by X-ray ionizations (Gredel & Dalgarno 1995). X-rays have been detected in very fast shocks in HH-objects (HH2A, Pravdo et al. 2001; HH 154, Bally et al. 2003). Pumping by Lyα photons of H_2 is possible in a warm gas that contains a fraction of H_2 in the $v' = 2$, $J' = 5$ level (Schwartz et al. 1987). The excitation of electronic states by UV or Lyα photons follows dipole selection rules, while the collisional excitation by secondary electrons does not. Non-thermal excitation of the ro-vibrational levels may also occur in a gas where H_2 reforms after the passage of a strong, dissociative shock (LeBourlot et al. 1995; Casu & Cecchi-Pestellini 2005; Tiné et al. 2003). In such models, uncertainties about whether the H_2 formation energy is equipartitioned among the ro-vibrational levels, the kinetic energy of the molecule, and the internal energy of the grain lattice, translate to significant differences in the modeled H_2 spectra. A comparison with the observations is thus difficult.

The shocked gas in molecular outflows from protostars may be affected by the non-thermal excitation scenarios described above. Fast, dissociative shocks produce a radiative precursor that contains a strong ultraviolet radiation field. Embedded TTau stars in the star-forming regions may contribute a significant X-ray radiation field to the environment (Guedel et al. 2007, and references therein). Non-thermal excitation scenarios introduce a pronounced dependence of the rotational and vibrational excitation temperatures of the ro-vibrational levels in the electronic ground state of H_2. This is evident in the strong deviations from the smooth Boltzmann distribution that characterizes thermal gas.

None of these effects dominate the excitation of H_2 in HH91A. What is immediately clear from the H_2 excitation diagram shown in Fig. 8, but more convincingly from the excellent agreement of the model H_2 emission spectra that arises from thermally excited gas and the observations, is that all ro-vibrational levels up to excitation energies of 40 000 K are in LTE. The fluxes in the high-excitation emission lines in the observed (6, 4), (7, 4), and (8, 4) bands are in excellent agreement with the expected strengths from the two-component thermal gas described above. The presence of these lines does not require the use of non-thermal excitation scenarios to explain the observed H_2 emission towards HH91A.

At kinetic temperatures of a few 1000 K, the rate coefficients for collisional excitation of H_2 by hydrogen atoms are of the order of 10^{-12} cm^{-3} s^{-1}. In order to estimate the extent to which the non-thermal excitation scenarios discussed above contribute to the H_2 excitation, we use the models of Gredel & Dalgarno (1995) to calculate the entry rates into the ro-vibrational levels of the ground state from X-ray and UV-fluorescence. X-ray ionization rates need to be significantly larger than $\zeta = 10^{-15}$ s^{-1} for collisional impact excitations of electronic H_2 states by fast secondary electrons to result in entry rates that exceed those from thermal excitations in a gas with a temperature of a few 1000 K. The generally adopted value of the cosmic-ray ionization rate in dense gas is $\zeta = 10^{-17}$ s^{-1}. The upper limit to the ionization fraction from X-rays is about $x_e \leq 10^{-4}$. It can thus be ruled out that

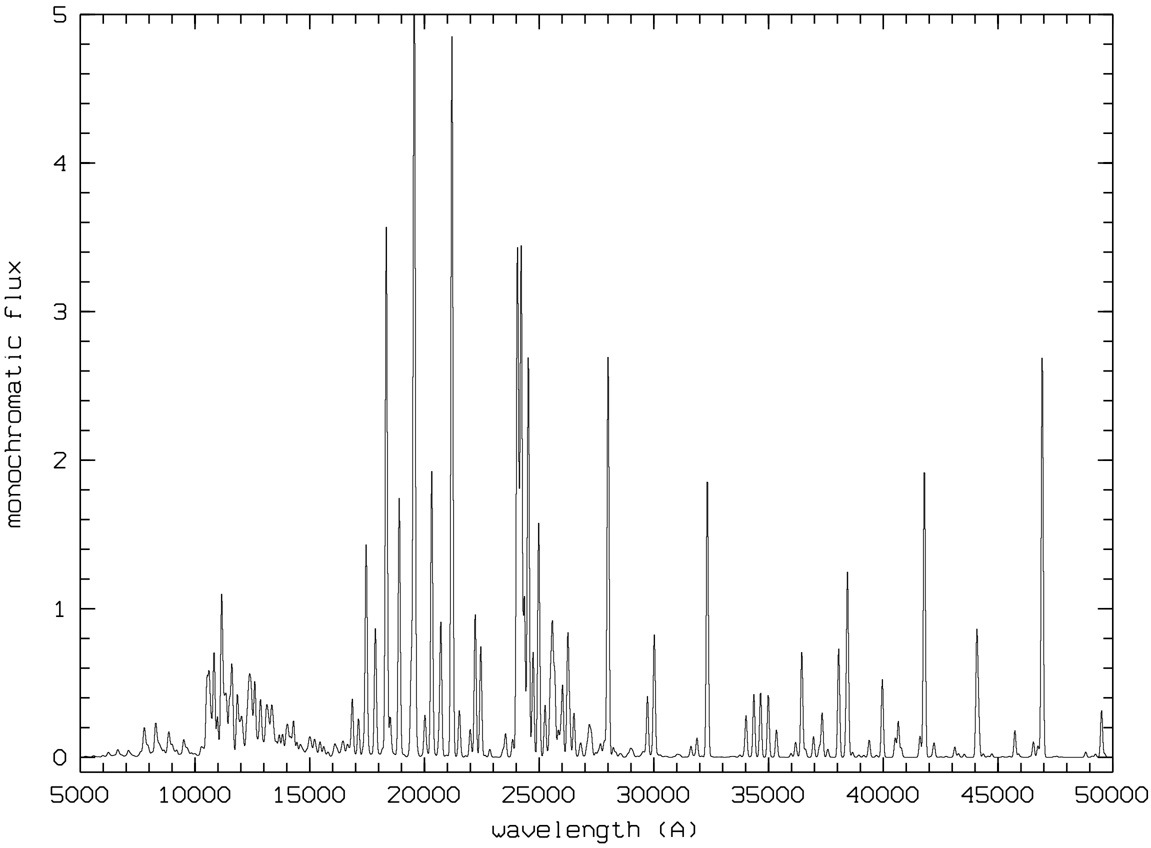

Fig. 9. Modeled H_2 emission spectrum that results from a total column of $N(H_2) = 10^{18}$ cm^{-2} of hot gas at a temperature of 2750 K, which contains a fraction of 1% of hot gas at 6000 K. Fluxes are in units of 10^{-19} W m^{-2} and wavelengths are in Å. Emission lines are Voigt line profiles at a FWHM of 200 Å.

X-rays contribute significantly to the H_2 emission observed towards HH91A. Similarly, a strong ultraviolet radiation field that exceeds the strength of the ambient interstellar radiation field by factors of several hundred is required for UV fluorescence to compete with the thermal population of H_2 levels in the ground state. The presence of a fast, dissociative shock with a strong UV precursor towards HH91A should thus be ruled out as well.

In order for the H_2 levels up to excitation energies of 30 000 cm^{-1} to be thermalized, very large densities in the compressed post-shock gas are required. The critical densities that are required to populate the ro-vibrational levels are equal to the Einstein A-values divided by the collisional de-excitation rate coefficients, $n_{\rm crit}(v'J') = A(v'J'v''J'')/\langle\sigma v\rangle$. The critical densities exceed values of $n_{\rm crit} > 10^7$ cm^{-3} for levels with excitation energies above 30 000 cm^{-1}. A more careful inspection of the H_2 excitation diagram shown in Fig. 8 shows that the population density among some of the very high-excitation levels, with excitation energies above 30 000 K, may show signs of sub-thermal excitation. In particular, the population density inferred from the optical (7, 3) S(11) line at 7978 Å, which has an excitation energy of 30 368 cm^{-1}, has a measured flux that is about a factor of three lower than what is expected from our two-component thermal model. This may indicate the onset of subthermal excitation for the very high levels, such as the $v' = 7, J' = 13$ level from which the (7, 3)S(11) line arises.

From the optical observations of [SII] 6717 Å and 6731 Å lines, Gredel et al. (1995) inferred very low electron densities of the order of $n_{\rm e} \approx 300$ cm^{-3} towards HH91A. This finding is consistent with the upper limit of the ionization fraction of 10^{-4} and the critical densities derived above. The absence of emission from [FeII] (e.g. the $a^4D_{7/2} - a^4F_{9/2}$ near 1.644 μm) supports the idea that H_2 is excited by a relatively slow, non-dissociative shock. Emission from ionized atomic species such as [FeII] is often observed in Herbig-Haro objects (e.g. Nisini et al. 2002), yet the strength of the atomic lines is not well reproduced by shock-models that explain the H_2 emission. This suggests that [FeII] arises from faster, dissociative shocks and in regions that are distinct from H_2-emitting regions. Weak emission from [CI] is seen near 8727 Å, with a flux of $F_{8727} \approx 0.8 \times 10^{-19}$ W m^{-2}, and near 9825 Å and 9851 Å of $F_{9825} = 10.8 \times 10^{-19}$ W m^{-2} and $F_{9851} = 37 \times 10^{-19}$ W m^{-2}. The observed [CI]8727/(9825+9851) line ratio of 0.02 is well reproduced by slow, non-dissociative shocks. We thus conclude that the emission seen towards HH91A is produced in a slow J-type shock. This picture is in agreement with the expectation that evolved outflows favor the formation of J-shocks (Caratti o Garatti 2006). It has been pointed out by Flower et al. (2003) that the discrimination between C-type and J-type shocks based on H_2 excitation diagrams is far from straightforward. A J-shock is preferred here because C-type shocks fail, in general, to produce the high degree of thermalization that is observed here. This conclusion is in agreement with earlier results by Smith (1994) whose analysis is based on fewer observed H_2 lines.

It is difficult to make firm statements regarding the possibility that the observed H_2 emission arises from molecules which reform after the passage of a fast, dissociative shock. The H_2 emissivities produced from reforming H_2 in diffuse and dense gas were calculated by Tiné et al. (2003) and by LeBourlot et al. (2002). Tiné et al. (2003) calculated an emission spectrum of H_2 produced via an Eley-Rideal process on graphite. In Fig. 9 we reproduce the H_2 emission spectrum that results from our two-component gas model (2750 K + 1% 6000 K). For the sake of simplicity, the width of the H_2 emission lines is kept constant at 200 Å over the spectral range of 5000 Å to 5 μm in Fig. 9. A comparison with Figs. 2 and 3 of Tiné et al. (2003) does not allow us to rule out the presence of re-forming H_2 molecules in HH91A, nor does it support the idea that reformation occurs. In particular, the very strong emission in the (0, 0) S(9) line predicted by Tiné et al. (2003) in their mechanism is also expected from thermal gas at 2750 K. The models presented by Casu & Cecchi-Pestellini (2005) predict very large column densities in very high rotational levels ($J > 20$) of H_2. The wavelengths of the very high rotational lines are not covered by our observations.

5. Conclusions

The findings presented here are summarized as follows:

1. From the analysis of some 200 emission lines of molecular hydrogen that are detected towards HH91A, it is concluded that the emission arises from thermally excited H_2, where the bulk of the gas is at a temperature of 2750 K and where 1% of the gas is at a temperature of 6000 K. The total column density of the shocked H_2 is $N(H_2) = 10^{18}$ cm^{-2}.
2. Emission from very high-excitation lines in the (6, 4), (6, 3), (7, 4), and (8, 4) bands is detected, with excitation energies of the corresponding ro-vibrational levels of up to 40 000 K. The fluxes in these high-excitation lines are consistent with the expectations of a thermally excited gas.
3. It is suggested that the H_2 emission arises from a slow, non-dissociative J-shock. A comparison with model calculations shows that contributions from non-thermal excitation scenarios, such as H_2 pumping by Lyα or UV radiation, or collisional excitations by non-thermal, fast electrons, are not significant.
4. The results concerning the presence of H_2 emission from re-forming molecules are inconclusive.

Acknowledgements. The insightful and constructive comments of the referee, Chris Davis, are gratefully acknowledged. The assistance of Nicolas Cardiel and Alberto Aguirre during the PMAS observations and of Sebastian Sanchez during the reduction of the PMAS data is acknowledged.

References

Bally, J., Feigelson, E., & Reipurth, B. 2003, ApJ, 584, 843
Cabrit, S., Flower, D. R., Pineau des Forêts, G., LeBourlot, J., & Ceccarelli, C. 2004, Ap&SS, 292, 501
Caratti o Garatti, A., Giannini, T., Nisini, B., & Lorenzetti, D. 2006, A&A, 449, 1077
Casu, S., & Cecchi-Pestellini, C. 2005, J. Phys. Conf. Ser., 6, 191
Davis, C. J., Mundt, R., & Eisloeffel, J. 1994, ApJ, 437, L55
Davis, C. J., Varricatt, W. P., Todd, S. P., & Ramsay Howat, S. K. 2004, A&A, 425, 981
Flower, D. R., LeBourlot, J., Pineau des Forêts, G., & Cabrit, S. 2003, MNRAS, 341, 70
Froebrich, D., Smith, M. D., Hodapp, K.-W., & Eisloeffel, J. 2003, MNRAS, 436, 163
Giannini, T., Nisini, B., Caratti o Garatti, A., & Lorenzetti, D. 2002, ApJ, 570, L33
Giannini, T., McCoey, C., Nisini, B., et al. 2006, A&A, 459, 821
Gredel, R. 1994, A&A, 292, 580
Gredel, R. 1996, A&A, 305, 582
Gredel, R. 2006, A&A, 457, 157
Gredel, R., & Dalgarno, A. 1995, ApJ, 446, 852
Gredel, R., Reipurth, B., & Heathcote, S. 1992, A&A, 266, 439
Guedel, M., Skinner, S. L., Mel'nikov, S. Yu., et al. 2006, A&A, 468, 529
LeBourlot, J., Pineau des Forêts, G., Roueff, E., Dalgarno, A., & Gredel, R. 1995, ApJ, 449, 178
LeBourlot, J., Pineau des Forêts, G., Flower, D. R., & Cabrit, S. 2002, MNRAS, 332, 985
McCartney, M. S. K., Brand, P. W. J. L., Burton, M. G., & Chrysostomou, A. 1999, MNRAS, 307, 315
McCoey, C., Giannini, T., Flower, D. R., & Caratti o Garatti, A. 2004, MNRAS, 353, 813
McKee, C. F., & Tan, J. C. 2003, ApJ, 569, 846
Moneti, A., & Reipurth, B. 1995, A&A, 301, 721
Nisini, B., Caratti o Garatti, A., Giannini, T., & Lorenzetti, D. 2002, A&A, 393, 1035
Pravdo, S. H., Feigelson, E. D., Garmire, G., et al. 2001, Nature, 413, 708
Roth, M. M., Fechner, T., Becker, T., & Kelz, A. 2004, SPIE, 5499, 387
Roth, M. M., Kelz, A., Fechner, T., et al. 2005, PASP, 117, 620
Schwartz, R. D., Cohen, M., & Williams, P. M. 1987, ApJ, 322, 403
Smith, M. D. 1994, A&A, 289, 256
Smith, M. D., O'Connell, B., & Davis, C. J. 2007, A&A, 466, 565
Tine, S., Lepp, S., Gredel, R., & Dalgarno, A. 1997, ApJ, 481, 282
Tine, S., Williams, D. A., Clary, D. C., et al. 2003, ApSS, 288, 377
Yorke, H. W., & Sonnenhalter, C. 2002, ApJ, 569, 846

Online Material

Table 2. Near-infrared line detections obtained with SOFI.

Line	Wavelength (Å)	Flux F (10^{-19} W m^{-2})	$N(v'J')$ (10^{14} cm^{-2})
grism GB order 1			
(6, 3)S(8)	0.953	4.7(1.0)	0.3 (0.1)
(6, 3)S(4)	0.959	1.7(1.0)	0.1 (0.0)
(6, 3)S(3)	0.966	4.1(1.0)	0.4 (0.1)
(7, 4)S(3)*	1.028	4.8(1.0)	0.3 (0.1)
(7, 4)S(5)*	1.029	4.8(1.0)	0.3 (0.1)
(5, 2)O(4)*	1.039	5.0(1.0)	6.0 (1.2)
(6, 3)Q(3)*	1.039	5.0(1.0)	1.4 (0.3)
(6, 3)S(15)*	1.040	5.0(1.0)	1.3 (0.3)
(2, 0)S(9)	1.054	75.8(7.6)	18.1 (3.6)
(2, 0)S(8)	1.058	23.0(2.3)	5.2 (1.0)
(2, 0)S(13)	1.061	7.6(1.0)	3.2 (0.6)
(2, 0)S(7)	1.064	78.4(7.8)	17.3 (3.5)
(2, 0)S(6)	1.073	30.1(3.0)	6.7 (1.3)
(2, 0)S(15)	1.078	≤1.2	≤0.9
(2, 0)S(5)	1.085	106.9(10.7)	24.8 (5.0)
(2, 0)S(4)	1.100	31.0(3.1)	7.8 (1.6)
(2, 0)S(3)	1.117	60.4(6.0)	17.1 (3.4)
(3, 1)S(9)*	1.120	29.7(3.0)	3.6 (0.7)
(3, 1)S(11)*	1.121	29.7(3.0)	4.7 (0.9)
(3, 1)S(8)	1.124	13.2(1.3)	1.5 (0.3)
(3, 1)S(7)	1.130	36.5(3.7)	3.9 (0.8)
(3, 1)S(13)	1.132	4.1(1.0)	1.0 (0.2)
(2, 0)S(2)	1.138	34.2(3.4)	11.4 (2.3)
(3, 1)S(6)	1.140	17.5(1.7)	1.8 (0.4)
(3, 1)S(5)	1.152	46.3(4.6)	5.0 (1.0)
(2, 0)S(1)	1.162	63.6(6.4)	27.2 (5.4)
(3, 1)S(4)	1.167	17.8(1.8)	2.0 (0.4)
(3, 1)S(3)	1.186	51.2(5.1)	6.4 (1.3)
(2, 0)S(0)	1.190	14.3(1.4)	9.3 (1.9)
(4, 2)S(9)*	1.196	5.6(1.0)	0.6 (0.1)
(4, 2)S(10)*	1.196	5.6(1.0)	0.7 (0.2)
(4, 2)S(8)*	1.199	3.7(1.0)	0.3 (0.1)
(4, 2)S(11)*	1.199	3.7(1.0)	0.5 (0.1)
(4, 2)S(7)	1.205	15.6(1.6)	1.2 (0.2)
(3, 1)S(2)	1.208	13.4(1.3)	2.0 (0.4)
(4, 2)S(6)	1.214	8.0(1.0)	0.6 (0.1)
(4, 2)S(5)	1.226	19.5(1.9)	1.5 (0.3)
(3, 1)S(1)	1.233	30.8(3.1)	5.7 (1.1)
(2, 0)Q(1)	1.238	39.7(4.0)	17.8 (3.6)
(2, 0)Q(2)*	1.242	21.2(2.1)	13.4 (2.7)
(4, 2)S(4)*	1.242	21.2(2.1)	1.7 (0.3)
(2, 0)Q(3)	1.247	41.8(4.2)	28.3 (5.7)
(2, 0)Q(4)	1.255	14.4(1.4)	10.1 (2.0)
(4, 2)S(3)	1.262	19.9(2.0)	1.7 (0.3)
(2, 0)Q(5)	1.264	38.6(3.9)	27.8 (5.6)
(2, 0)Q(6)	1.274	9.6(1.0)	7.1 (1.4)
(5, 3)S(9)	1.282	3.9(1.0)	0.4 (0.1)
(4, 2)S(2)*	1.285	7.7(1.0)	0.8 (0.2)
(5, 3)S(10)*	1.284	7.7(1.0)	0.9 (0.2)
(2, 0)Q(7)*	1.287	29.5(3.0)	22.3 (4.5)
(5, 3)S(7)*	1.289	29.5(3.0)	2.2 (0.4)
(2, 0)O(2)	1.293	7.3(1.0)	1.9 (0.4)
(5, 3)S(6)	1.298	2.9(1.0)	0.2 (0.0)
(2, 0)Q(8)	1.302	6.5(1.0)	5.1 (1.0)
(4, 2)S(1)	1.312	19.8(2.0)	2.4 (0.5)
(3, 1)Q(1)	1.314	15.1(1.5)	2.8 (0.6)
(5, 3)S(5)	1.311	4.0(1.0)	0.3 (0.1)
(3, 1)Q(2)*	1.318	15.9(1.6)	4.1 (0.8)
(2, 0)Q(9)*	1.319	15.9(1.6)	12.6 (2.5)
(3, 1)Q(3)	1.324	15.1(1.5)	4.2 (0.8)
(5, 3)S(4)	1.327	2.9(1.0)	0.2 (0.0)
(3, 1)Q(4)	1.332	6.0(1.0)	1.7 (0.3)
(2, 0)O(3)	1.335	32.2(3.2)	18.7 (3.7)
(2, 0)Q(10)	1.338	4.2(1.0)	3.5 (0.7)
(3, 1)Q(5)	1.342	24.3(2.4)	7.3 (1.5)
(5, 3)S(3)	1.347	8.1(1.0)	0.6 (0.1)
(2, 0)Q(12)*	1.381	7.6(1.0)	6.7 (1.3)
(2, 0)O(4)*	1.382	7.6(1.0)	7.1 (1.4)
(6, 4)S(8)*	1.384	2.2(1.0)	0.2 (0.1)
(6, 4)S(9)*	1.384	2.2(1.0)	0.3 (0.1)
(6, 4)S(10)*	1.389	2.2(1.0)	0.4 (0.1)
(6, 4)S(7)*	1.388	2.2(1.0)	0.2 (0.0)
(3, 1)Q(9)	1.403	9.7(1.0)	3.3 (0.7)
(6, 4)S(5)	1.408	4.1(1.0)	0.3 (0.1)
(3, 1)O(3)*	1.418	6.8(1.0)	1.6 (0.3)
(4, 2)Q(4)*	1.418	6.8(1.0)	1.3 (0.3)
(3, 1)Q(10)*	1.424	6.3(1.0)	2.2 (0.4)
(6, 4)S(4)*	1.425	6.3(1.0)	0.4 (0.1)
(4, 2)Q(5)	1.430	7.1(1.0)	1.4 (0.3)
(2, 0)O(5)	1.432	14.0(1.4)	20.1 (4.0)
(4, 2)Q(6)	1.443	3.1(1.0)	0.6 (0.2)
(3, 1)Q(11)	1.448	9.2(1.0)	3.3 (0.7)
(4, 2)Q(7)	1.459	7.3(1.0)	1.5 (0.3)
(2, 0)Q(15)	1.465	1.7(1.0)	1.8 (1.0)
(3, 1)O(4)	1.468	2.5(1.0)	0.9 (0.4)
(3, 1)Q(12)	1.474	1.7(1.0)	0.7 (0.4)
(2, 0)O(6)	1.487	3.2(1.0)	7.1 (2.4)
(5, 3)Q(1)	1.493	1.9(1.0)	0.2 (0.1)
(4, 2)Q(9)	1.499	6.1(1.0)	1.3 (0.3)
(3, 1)Q(13)	1.502	6.7(1.0)	2.7 (0.5)
(5, 3)Q(3)*	1.506	3.8(1.0)	0.5 (0.1)
(7, 5)S(7)*	1.506	3.8(1.0)	0.4 (0.1)
(4, 2)O(3)	1.510	5.4(1.0)	0.7 (0.2)
(5, 3)Q(4)	1.516	2.0(1.0)	0.3 (0.2)
(3, 1)O(5)	1.522	13.4(1.3)	7.2 (1.4)
(3, 1)Q(14)	1.533	4.0(1.0)	1.7 (0.2)
(5, 3)Q(5)	1.529	4.9(1.0)	0.7 (0.1)
(2, 0)O(7)	1.546	8.6(1.0)	29.6 (5.9)
(4, 2)Q(11)	1.549	3.6(1.0)	0.9 (0.2)
(7, 5)S(3)	1.562	4.5(1.0)	0.4 (0.1)
(4, 2)O(4)	1.564	2.9(1.0)	0.6 (0.1)
(3, 1)Q(15)	1.569	2.0(1.0)	0.9 (0.2)
(5, 3)Q(8)	1.584	2.3(1.0)	0.4 (0.1)
(6, 4)Q(1)	1.602	≤1.0	≤0.1
(5, 3)Q(9)	1.608	3.2(1.0)	0.6 (0.2)
(2, 0)O(8)*	1.610	4.0(1.0)	22.1 (5.0)
(4, 2)Q(13)*	1.612	4.0(1.0)	1.1 (0.2)
(6, 4)Q(3)	1.616	2.2(1.0)	0.3 (0.1)
(4, 2)O(5)	1.622	4.7(1.0)	1.4 (0.3)
grism HR order 2			
(3, 1)O(5)	1.522	8.4(0.8)	4.5 (0.9)
(2, 0)O(7)	1.546	4.7(0.5)	16.3 (3.3)
(4, 2)Q(11)	1.549	2.4(0.5)	0.6 (0.1)
(5, 3)O(2)*	1.561	1.8(0.5)	0.1 (0.0)
(7, 5)S(3)*	1.562	1.8(0.5)	0.1 (0.0)
(5, 3)Q(7)	1.563	2.5(0.5)	0.4 (0.1)
(5, 3)Q(9)	1.608	1.5(0.5)	0.3 (0.1)
(4, 2)Q(13)	1.612	1.6(0.5)	0.4 (0.1)
(6, 4)Q(3)*	1.616	1.0(0.5)	0.1 (0.0)
(2, 0)Q(19)*	1.616	1.0(0.5)	1.4 (0.3)
(7, 5)S(1)	1.620	1.0(0.5)	0.1 (0.0)
(6, 4)Q(5)	1.643	1.3(0.5)	0.2(0.0)
(3, 1)O(7)	1.645	3.8(0.5)	4.6 (0.9)
(3, 1)Q(17)	1.648	1.4(0.5)	0.7 (0.2)

Table 2. continued.

Line	Wavelength (Å)	Flux *F* (10^{-19} W m^{-2})	$N(v'J')$ (10^{14} cm^{-2})
(4, 2)Q(14)	1.649	1.7(0.5)	0.5 (0.1)
(1, 0)S(11)	1.650	4.3(0.5)	9.2 (1.8)
(1, 0)S(18)	1.659	≤0.5	≤0.2
(6, 4)Q(6)	1.661	≤0.5	≤0.1
(1, 0)S(10)	1.666	6.4(0.6)	7.1 (1.4)
(1, 0)S(19)	1.675	1.5(0.5)	0.4 (0.1)
(6, 4)Q(7)	1.683	2.5(0.5)	0.4 (0.1)
(1, 0)S(9)	1.688	44.9(4.5)	31.6 (6.3)
(1, 0)S(8)	1.715	28.2(2.8)	14.4 (2.9)
(2, 1)S(9)	1.790	12.5(1.3)	10.4 (2.1)
(6, 4)O(3)	1.733	1.2(0.5)	0.1 (0.0)
(5, 3)O(5)	1.736	2.0(0.5)	0.4 (0.1)
(6, 4)Q(9)	1.737	2.0(0.5)	0.3 (0.1)
(2, 1)S(15)	1.739	5.1(0.5)	3.4 (0.7)
(5, 3)Q(13)	1.741	2.0(0.5)	0.4 (0.1)
(1, 0)S(7)	1.748	162.4(16.2)	66.6 (13.3)
(2, 1)S(11)	1.753	2.0(0.5)	11.9 (2.4)
(4, 2)O(7)	1.756	4.0(0.5)	2.6 (0.5)
(2, 1)S(17)	1.759	4.0(0.5)	0.9 (0.2)
(1, 0)S(6)	1.788	95.9(9.6)	33.9 (6.8)
(2, 1)S(9)	1.790	10.0(1.0)	8.3 (1.7)
grism HR order 1			
(2, 1)S(4)	2.004	19.4(1.9)	4.9 (2.4)
(1, 0)S(2)	2.034	272.4(27.2)	97.4 (48.7)
(3, 2)S(5)	2.066	14.9(1.5)	4.8 (2.4)
(2, 1)S(3)	2.074	103.1(10.3)	25.9 (13.0)
(1, 0)S(1)	2.122	647.9(64.8)	277.3 (55.5)
(3, 2)S(4)	2.128	4.0(1.0)	1.1(0.3)
(2, 1)S(2)	2.154	36.4(3.6)	9.8 (2.0)
(3, 2)S(3)	2.201	21.9(2.2)	6.0 (1.2)
(1, 0)S(0)	2.223	130.5(13.0)	80.4 (16.1)
(2, 1)S(1)	2.248	90.6(9.1)	28.7 (5.7)
(4, 3)S(4)	2.267	4.0 (1.0)	8 1.6 (0.3)
(3, 2)S(2)	2.287	4.5(1.0)	1.3 (0.3)

∗ Unresolved line blend.

Table 3. Theoretical H_2 line fluxes.

Line	Wavelength (μm)	$E_{\rm up}$ (cm^{-1})	$F_{2750\ \rm K}$ (10^{-19} W m^{-2})	$F_{6000\ \rm K}$ (10^{-19} W m^{-2})	$F_{\rm tot}$ (10^{-19} W m^{-2})
(0, 0)S(2)	12.279	1168.8	2.5	0.0	2.5
(0, 0)S(3)	9.665	1740.2	30.8	0.5	31.3
(0, 0)S(4)	8.026	2414.8	27.6	0.5	28.1
(0, 0)S(5)	6.909	3187.6	164.8	4.1	168.8
(0, 0)S(6)	6.109	4051.7	87.0	2.7	89.7
(0, 0)S(7)	5.511	5002.0	344.7	14.2	358.9
(0, 0)S(8)	5.053	6030.8	130.7	7.2	137.9
(0, 0)S(9)	4.695	7132.0	393.4	29.7	423.1
(0, 0)S(10)	4.410	8298.6	118.3	12.4	130.7
(0, 0)S(11)	4.181	9523.8	291.7	43.4	335.1
(0, 0)S(12)	3.998	10800.0	73.8	15.8	89.6
(0, 0)S(13)	3.846	12123.7	156.8	48.7	205.5
(0, 0)S(14)	3.736	13477.0	34.9	15.9	50.8
(0, 0)S(15)	3.647	14866.0	66.2	44.7	111.0
(0, 0)S(16)	3.536	16304.8	13.3	13.5	26.9
(0, 0)S(17)	3.467	17750.2	23.2	35.5	58.8
(0, 0)S(18)	3.438	19213.2	4.3	10.0	14.3
(0, 0)S(19)	3.404	20688.0	7.0	24.7	31.7
(1, 0)O(2)	2.627	4161.1	84.0	2.7	86.8
(1, 0)Q(1)	2.407	4273.8	391.1	13.1	404.2
(1, 0)O(3)	2.803	4273.8	330.7	11.1	341.8
(1, 0)S(0)	2.223	4497.8	123.2	4.4	127.6
(1, 0)Q(2)	2.413	4497.8	136.1	4.9	141.0
(1, 0)O(4)	3.004	4497.8	104.6	3.7	108.3
(1, 0)S(1)	2.122	4831.4	625.5	24.6	650.1
(1, 0)Q(3)	2.424	4831.4	439.0	17.3	456.3
(1, 0)O(5)	3.235	4831.4	246.3	9.7	255.9
(1, 0)S(2)	2.034	5271.4	254.9	11.4	266.3
(1, 0)Q(4)	2.437	5271.4	141.6	6.3	147.9
(1, 0)O(6)	3.501	5271.4	55.7	2.5	58.2
(1, 0)S(3)	1.958	5813.9	772.5	40.1	812.6
(1, 0)Q(5)	2.455	5813.9	372.7	19.4	392.1
(1, 0)O(7)	3.808	5813.9	100.2	5.2	105.5
(1, 0)S(4)	1.892	6454.3	224.3	14.0	238.2
(1, 0)Q(6)	2.476	6454.3	100.0	6.2	106.2
(1, 0)O(8)	4.162	6454.3	17.9	1.1	19.0
(1, 0)S(5)	1.836	7187.4	514.7	39.5	554.1
(1, 0)Q(7)	2.500	7187.4	223.6	17.1	240.7
(1, 0)O(9)	4.576	7187.4	26.0	2.0	27.9
(1, 0)S(6)	1.788	8007.8	116.3	11.2	127.5
(1, 0)Q(8)	2.528	8007.8	51.8	5.0	56.8
(1, 0)O(10)	5.058	8007.8	3.8	0.4	4.2
(1, 0)S(7)	1.748	8908.3	209.8	26.2	236.0
(1, 0)Q(9)	2.560	8908.3	101.5	12.7	114.2
(1, 0)O(11)	5.630	8908.3	4.5	0.6	5.1
(1, 0)S(8)	1.715	9883.8	37.1	6.1	43.3
(1, 0)Q(10)	2.595	9883.8	20.9	3.4	24.3
(1, 0)S(9)	1.688	10927.1	51.5	11.4	62.9
(1, 0)Q(11)	2.635	10927.1	36.7	8.1	44.8
(1, 0)S(10)	1.666	12031.4	6.7	2.0	8.7
(1, 0)Q(12)	2.679	12031.4	6.8	2.1	8.9
(1, 0)S(11)	1.650	13191.1	6.0	2.5	8.5
(1, 0)Q(13)	2.727	13191.1	10.9	4.6	15.5
(1, 0)Q(14)	2.778	14399.1	1.9	1.1	3.0
(1, 0)Q(15)	2.836	15649.6	2.8	2.4	5.1
(1, 0)S(15)	1.631	18253.5	0.4	0.8	1.2
(1, 0)Q(17)	2.952	18253.5	0.6	1.1	1.7
(1, 0)S(17)	1.642	20957.7	0.5	2.0	2.6
(1, 0)S(19)	1.675	23720.3	0.3	2.6	2.9
(1, 1)S(3)	10.178	5813.9	3.3	0.2	3.4
(1, 1)S(4)	8.454	6454.3	2.9	0.2	3.1

Table 3. continued.

Line	Wavelength (μm)	E_{up} (cm^{-1})	$F_{2750\ \mathrm{K}}$ (10^{-19} W m^{-2})	$F_{6000\ \mathrm{K}}$ (10^{-19} W m^{-2})	F_{tot} (10^{-19} W m^{-2})
(1, 1)S(5)	7.281	7187.4	17.8	1.4	19.2
(1, 1)S(6)	6.437	8007.8	9.6	0.9	10.5
(1, 1)S(7)	5.811	8908.3	38.5	4.8	43.3
(1, 1)S(8)	5.330	9883.8	14.9	2.4	17.3
(1, 1)S(9)	4.953	10927.1	45.7	10.1	55.8
(1, 1)S(10)	4.656	12031.4	14.0	4.2	18.3
(1, 1)S(11)	4.417	13191.1	35.4	14.9	50.3
(1, 1)S(12)	4.224	14399.1	9.2	5.4	14.6
(1, 1)S(13)	4.067	15649.6	20.0	16.9	36.9
(1, 1)S(14)	3.941	16936.2	4.6	5.5	10.1
(1, 1)S(15)	3.840	18253.5	8.9	15.7	24.6
(1, 1)S(16)	3.760	19595.7	1.8	4.7	6.6
(1, 1)S(17)	3.698	20957.7	3.3	12.5	15.8
(1, 1)S(18)	3.652	22333.8	0.6	3.5	4.2
(1, 1)S(19)	3.620	23720.3	1.1	8.8	9.9
(1, 1)S(20)	3.600	25111.6	0.2	2.4	2.6
(2, 0)O(2)	1.293	8086.9	8.9	0.9	9.8
(2, 0)Q(1)	1.238	8193.8	44.2	4.5	48.7
(2, 0)O(3)	1.335	8193.8	33.9	3.5	37.4
(2, 0)S(0)	1.190	8406.3	15.0	1.6	16.7
(2, 0)Q(2)	1.242	8406.3	15.6	1.7	17.3
(2, 0)O(4)	1.382	8406.3	10.5	1.1	11.6
(2, 0)S(1)	1.162	8722.7	81.6	9.7	91.3
(2, 0)Q(3)	1.247	8722.7	51.5	6.1	57.6
(2, 0)O(5)	1.432	8722.7	24.3	2.9	27.2
(2, 0)S(2)	1.138	9139.9	36.0	4.8	40.8
(2, 0)Q(4)	1.255	9139.9	17.1	2.3	19.4
(2, 0)O(6)	1.487	9139.9	5.4	0.7	6.2
(2, 0)S(3)	1.117	9654.1	119.4	18.4	137.9
(2, 0)Q(5)	1.264	9654.1	46.8	7.2	54.0
(2, 0)O(7)	1.546	9654.1	9.8	1.5	11.3
(2, 0)S(4)	1.100	10261.2	38.6	7.1	45.7
(2, 0)Q(6)	1.274	10261.2	13.1	2.4	15.5
(2, 0)O(8)	1.610	10261.2	1.8	0.3	2.1
(2, 0)S(5)	1.085	10955.7	100.5	22.4	122.9
(2, 0)Q(7)	1.287	10955.7	30.8	6.9	37.7
(2, 0)O(9)	1.680	10955.7	2.6	0.6	3.1
(2, 0)S(6)	1.073	11732.1	26.4	7.3	33.7
(2, 0)Q(8)	1.302	11732.1	7.6	2.1	9.7
(2, 0)S(7)	1.064	12584.8	57.2	20.2	77.4
(2, 0)Q(9)	1.319	12584.8	15.8	5.6	21.4
(2, 0)S(8)	1.058	13507.4	12.7	5.8	18.5
(2, 0)Q(10)	1.338	13507.4	3.5	1.6	5.1
(2, 0)S(9)	1.054	14493.6	23.5	14.3	37.8
(2, 0)Q(11)	1.358	14493.6	6.6	4.0	10.6
(2, 0)S(10)	1.052	15537.1	4.5	3.7	8.2
(2, 0)Q(12)	1.381	15537.1	1.3	1.1	2.4
(2, 0)S(11)	1.053	16632.1	7.3	8.1	15.4
(2, 0)Q(13)	1.407	16632.1	2.3	2.6	4.9
(2, 0)S(12)	1.056	17771.7	1.2	1.9	3.1
(2, 0)Q(14)	1.434	17771.7	0.4	0.7	1.1
(2, 0)S(13)	1.061	18950.3	1.7	3.7	5.4
(2, 0)Q(15)	1.465	18950.3	0.7	1.5	2.3
(2, 0)S(14)	1.068	20161.8	0.2	0.8	1.0
(2, 0)S(15)	1.078	21400.9	0.3	1.3	1.6
(2, 0)Q(17)	1.530	21400.9	0.2	0.9	1.1
(2, 1)O(2)	2.786	8086.9	15.3	1.5	16.8
(2, 1)Q(1)	2.551	8193.8	70.4	7.2	77.6
(2, 1)O(3)	2.974	8193.8	60.6	6.2	66.8
(2, 1)S(0)	2.356	8406.3	21.9	2.4	24.3
(2, 1)Q(2)	2.559	8406.3	24.6	2.7	27.3
(2, 1)O(4)	3.190	8406.3	19.4	2.1	21.4
(2, 1)S(1)	2.248	8722.7	110.5	13.1	123.6
(2, 1)Q(3)	2.570	8722.7	80.0	9.5	89.4

Table 3. continued.

Line	Wavelength (μm)	E_{up} (cm^{-1})	$F_{2750\ \mathrm{K}}$ (10^{-19} W m^{-2})	$F_{6000\ \mathrm{K}}$ (10^{-19} W m^{-2})	F_{tot} (10^{-19} W m^{-2})
(2, 1)O(5)	3.438	8722.7	46.0	5.5	51.5
(2, 1)S(2)	2.154	9139.9	44.7	6.0	50.6
(2, 1)Q(4)	2.585	9139.9	26.0	3.5	29.5
(2, 1)O(6)	3.724	9139.9	10.5	1.4	11.9
(2, 1)S(3)	2.074	9654.1	134.1	20.7	154.8
(2, 1)Q(5)	2.604	9654.1	69.2	10.7	79.9
(2, 1)O(7)	4.054	9654.1	19.2	3.0	22.1
(2, 1)S(4)	2.004	10261.2	38.4	7.0	45.5
(2, 1)Q(6)	2.627	10261.2	18.8	3.4	22.3
(2, 1)O(8)	4.438	10261.2	3.5	0.6	4.1
(2, 1)S(5)	1.945	10955.7	86.6	19.3	105.9
(2, 1)Q(7)	2.654	10955.7	42.7	9.5	52.2
(2, 1)O(9)	4.884	10955.7	5.1	1.1	6.2
(2, 1)S(6)	1.895	11732.1	19.0	5.3	24.3
(2, 1)Q(8)	2.685	11732.1	10.1	2.8	12.9
(2, 1)S(7)	1.853	12584.8	33.0	11.7	44.7
(2, 1)Q(9)	2.720	12584.8	20.1	7.1	27.2
(2, 1)O(11)	6.033	12584.8	0.9	0.3	1.2
(2, 1)S(8)	1.818	13507.4	5.5	2.5	8.0
(2, 1)Q(10)	2.760	13507.4	4.2	1.9	6.1
(2, 1)S(9)	1.790	14493.6	6.8	4.1	10.9
(2, 1)Q(11)	2.804	14493.6	7.5	4.6	12.1
(2, 1)S(10)	1.769	15537.1	0.7	0.6	1.3
(2, 1)Q(12)	2.852	15537.1	1.4	1.2	2.6
(2, 1)Q(13)	2.906	16632.1	2.3	2.6	5.0
(2, 1)Q(14)	2.965	17771.7	0.4	0.6	1.0
(2, 1)Q(15)	3.030	18950.3	0.6	1.3	2.0
(2, 1)S(15)	1.739	21400.9	0.3	1.5	1.8
(2, 1)S(17)	1.759	23939.6	0.3	2.5	2.8
(2, 1)S(19)	1.796	26524.8	0.2	2.8	3.0
(2, 2)S(5)	7.683	10955.7	2.1	0.5	2.6
(2, 2)S(6)	6.798	11732.1	1.1	0.3	1.5
(2, 2)S(7)	6.138	12584.8	4.7	1.7	6.4
(2, 2)S(8)	5.633	13507.4	1.9	0.9	2.7
(2, 2)S(9)	5.239	14493.6	5.8	3.5	9.3
(2, 2)S(10)	4.927	15537.1	1.8	1.5	3.3
(2, 2)S(11)	4.676	16632.1	4.7	5.2	9.9
(2, 2)S(12)	4.475	17771.7	1.2	1.9	3.2
(2, 2)S(13)	4.314	18950.3	2.8	6.0	8.7
(2, 2)S(14)	4.184	20161.8	0.6	2.0	2.6
(2, 2)S(15)	4.081	21400.9	1.3	5.6	6.9
(2, 2)S(16)	4.000	22661.7	0.3	1.7	2.0
(2, 2)S(17)	3.939	23939.6	0.5	4.5	5.0
(2, 2)S(18)	3.896	25228.7	0.1	1.3	1.4
(2, 2)S(19)	3.868	26524.8	0.2	3.1	3.3
(3, 0)Q(1)	0.850	11883.5	1.3	0.4	1.6
(3, 0)S(1)	0.815	12384.1	3.3	1.1	4.4
(3, 0)Q(3)	0.856	12384.1	1.5	0.5	2.0
(3, 0)S(2)	0.805	12778.8	1.6	0.6	2.2
(3, 0)S(3)	0.796	13265.3	6.0	2.6	8.5
(3, 0)Q(5)	0.868	13265.3	1.4	0.6	2.1
(3, 0)S(4)	0.789	13839.2	2.1	1.1	3.2
(3, 0)S(5)	0.784	14495.5	6.1	3.7	9.8
(3, 0)Q(7)	0.884	14495.5	1.0	0.6	1.6
(3, 0)S(6)	0.780	15228.9	1.7	1.3	3.1
(3, 0)S(7)	0.778	16033.8	4.2	3.9	8.1
(3, 0)Q(9)	0.906	16033.8	0.6	0.5	1.1
(3, 0)S(8)	0.778	16904.0	1.0	1.2	2.2
(3, 0)S(9)	0.779	17833.8	2.1	3.3	5.3
(3, 0)S(10)	0.782	18816.8	0.4	0.9	1.4
(3, 0)S(11)	0.786	19847.1	0.8	2.2	3.0
(3, 0)S(13)	0.800	22025.0	0.2	1.3	1.5
(3, 1)O(2)	1.373	11782.4	3.2	0.9	4.1

Table 3. continued.

Line	Wavelength (μm)	$E_{\rm up}$ (cm^{-1})	$F_{2750\ \rm K}$ (10^{-19} W m^{-2})	$F_{6000\ \rm K}$ (10^{-19} W m^{-2})	$F_{\rm tot}$ (10^{-19} W m^{-2})
(3, 1)Q(1)	1.314	11883.5	15.5	4.5	20.0
(3, 1)O(3)	1.418	11883.5	12.5	3.6	16.2
(3, 1)S(0)	1.262	12084.7	5.2	1.6	6.8
(3, 1)Q(2)	1.318	12084.7	5.5	1.7	7.2
(3, 1)O(4)	1.468	12084.7	4.0	1.2	5.2
(3, 1)S(1)	1.233	12384.1	27.9	9.3	37.2
(3, 1)Q(3)	1.324	12384.1	18.3	6.1	24.5
(3, 1)O(5)	1.522	12384.1	9.6	3.2	12.8
(3, 1)S(2)	1.208	12778.8	12.2	4.6	16.8
(3, 1)Q(4)	1.332	12778.8	6.2	2.3	8.5
(3, 1)O(6)	1.581	12778.8	2.2	0.8	3.1
(3, 1)S(3)	1.186	13265.3	40.5	17.4	57.9
(3, 1)Q(5)	1.342	13265.3	17.0	7.3	24.3
(3, 1)O(7)	1.645	13265.3	4.2	1.8	6.0
(3, 1)S(4)	1.167	13839.2	13.1	6.6	19.7
(3, 1)Q(6)	1.354	13839.2	4.8	2.4	7.3
(3, 1)O(8)	1.715	13839.2	0.8	0.4	1.2
(3, 1)S(5)	1.152	14495.5	34.1	20.8	54.9
(3, 1)Q(7)	1.368	14495.5	11.6	7.0	18.6
(3, 1)O(9)	1.790	14495.5	1.3	0.8	2.0
(3, 1)S(6)	1.140	15228.9	9.0	6.7	15.7
(3, 1)Q(8)	1.385	15228.9	2.9	2.2	5.1
(3, 1)S(7)	1.130	16033.8	19.5	18.4	37.9
(3, 1)Q(9)	1.403	16033.8	6.2	5.8	12.0
(3, 1)S(8)	1.124	16904.0	4.4	5.2	9.6
(3, 1)Q(10)	1.424	16904.0	1.4	1.7	3.1
(3, 1)S(9)	1.120	17833.8	8.1	12.7	20.8
(3, 1)Q(11)	1.448	17833.8	2.7	4.2	6.9
(3, 1)S(10)	1.119	18816.8	1.6	3.2	4.8
(3, 1)Q(12)	1.474	18816.8	0.6	1.2	1.7
(3, 1)S(11)	1.121	19847.1	2.5	6.9	9.4
(3, 1)Q(13)	1.502	19847.1	1.0	2.8	3.8
(3, 1)S(12)	1.125	20918.2	0.4	1.6	2.0
(3, 1)S(13)	1.132	22025.0	0.6	2.9	3.5
(3, 1)Q(15)	1.569	22025.0	0.3	1.7	2.0
(3, 1)Q(17)	1.648	24321.2	0.1	1.0	1.0
(3, 2)O(2)	2.962	11782.4	2.3	0.6	2.9
(3, 2)Q(1)	2.710	11883.5	10.4	3.0	13.4
(3, 2)O(3)	3.164	11883.5	9.1	2.6	11.8
(3, 2)S(0)	2.501	12084.7	3.2	1.0	4.2
(3, 2)Q(2)	2.719	12084.7	3.6	1.1	4.8
(3, 2)O(4)	3.396	12084.7	2.9	0.9	3.8
(3, 2)S(1)	2.386	12384.1	15.9	5.3	21.2
(3, 2)Q(3)	2.731	12384.1	11.9	4.0	15.9
(3, 2)O(5)	3.663	12384.1	7.1	2.4	9.4
(3, 2)S(2)	2.287	12778.8	6.3	2.4	8.7
(3, 2)Q(4)	2.748	12778.8	3.9	1.5	5.4
(3, 2)O(6)	3.972	12778.8	1.6	0.6	2.2
(3, 2)S(3)	2.201	13265.3	18.7	8.0	26.7
(3, 2)Q(5)	2.769	13265.3	10.5	4.5	15.0
(3, 2)O(7)	4.330	13265.3	3.0	1.3	4.3
(3, 2)S(4)	2.128	13839.2	5.2	2.6	7.9
(3, 2)Q(6)	2.795	13839.2	2.9	1.5	4.3
(3, 2)S(5)	2.066	14495.5	11.4	7.0	18.4
(3, 2)Q(7)	2.825	14495.5	6.6	4.0	10.7
(3, 2)O(9)	5.234	14495.5	0.8	0.5	1.3
(3, 2)S(6)	2.013	15228.9	2.4	1.8	4.2
(3, 2)Q(8)	2.860	15228.9	1.6	1.2	2.8
(3, 2)S(7)	1.969	16033.8	3.8	3.6	7.5
(3, 2)Q(9)	2.899	16033.8	3.2	3.0	6.2
(3, 2)S(8)	1.934	16904.0	0.6	0.7	1.2
(3, 2)Q(10)	2.944	16904.0	0.7	0.8	1.5
(3, 2)S(9)	1.905	17833.8	0.5	0.8	1.4
(3, 2)Q(11)	2.994	17833.8	1.2	2.0	3.2
(3, 2)Q(13)	3.110	19847.1	0.4	1.1	1.5

Table 3. continued.

Line	Wavelength (μm)	E_{up} (cm^{-1})	$F_{2750\ \mathrm{K}}$ (10^{-19} W m^{-2})	$F_{6000\ \mathrm{K}}$ (10^{-19} W m^{-2})	F_{tot} (10^{-19} W m^{-2})
(3, 2)S(15)	1.862	24321.2	0.2	1.6	1.8
(3, 2)S(17)	1.890	26691.8	0.1	2.2	2.3
(3, 2)S(19)	1.940	29095.0	0.1	2.2	2.3
(3, 3)S(7)	6.500	16033.8	0.6	0.6	1.2
(3, 3)S(9)	5.556	17833.8	0.8	1.2	2.0
(3, 3)S(11)	4.967	19847.1	0.7	1.9	2.5
(3, 3)S(13)	4.592	22025.0	0.4	2.1	2.5
(3, 3)S(15)	4.355	24321.2	0.2	2.0	2.2
(3, 3)S(17)	4.218	26691.8	0.1	1.6	1.7
(3, 3)S(19)	4.161	29095.0	0.0	1.1	1.1
(4, 1)Q(1)	0.903	15345.8	0.7	0.5	1.2
(4, 1)S(1)	0.866	15818.3	1.7	1.5	3.3
(4, 1)Q(3)	0.910	15818.3	0.8	0.7	1.6
(4, 1)S(2)	0.855	16190.7	0.8	0.8	1.7
(4, 1)S(3)	0.846	16649.5	3.1	3.5	6.5
(4, 1)Q(5)	0.923	16649.5	0.8	0.9	1.8
(4, 1)S(4)	0.839	17190.4	1.1	1.4	2.5
(4, 1)S(5)	0.834	17808.8	3.2	4.9	8.1
(4, 1)Q(7)	0.942	17808.8	0.6	0.9	1.5
(4, 1)S(6)	0.830	18499.1	0.9	1.7	2.6
(4, 1)S(7)	0.829	19256.4	2.2	5.1	7.3
(4, 1)Q(9)	0.966	19256.4	0.4	0.8	1.2
(4, 1)S(8)	0.829	20074.5	0.5	1.6	2.1
(4, 1)S(9)	0.831	20947.5	1.1	4.2	5.4
(4, 1)S(10)	0.834	21869.5	0.2	1.2	1.4
(4, 1)S(11)	0.840	22834.6	0.4	2.9	3.3
(4, 1)S(13)	0.856	24870.3	0.1	1.6	1.8
(4, 2)O(2)	1.461	15250.3	0.9	0.6	1.5
(4, 2)Q(1)	1.398	15345.8	4.0	3.1	7.1
(4, 2)O(3)	1.510	15345.8	3.4	2.6	6.0
(4, 2)S(0)	1.343	15535.7	1.3	1.1	2.4
(4, 2)Q(2)	1.403	15535.7	1.4	1.2	2.6
(4, 2)O(4)	1.564	15535.7	1.1	0.9	2.0
(4, 2)S(1)	1.312	15818.3	7.0	6.2	13.2
(4, 2)Q(3)	1.409	15818.3	4.8	4.3	9.1
(4, 2)O(5)	1.622	15818.3	2.8	2.4	5.2
(4, 2)S(2)	1.285	16190.7	3.1	3.0	6.1
(4, 2)Q(4)	1.418	16190.7	1.6	1.6	3.2
(4, 2)O(6)	1.686	16190.7	0.7	0.7	1.3
(4, 2)S(3)	1.262	16649.5	10.1	11.3	21.4
(4, 2)Q(5)	1.430	16649.5	4.6	5.1	9.7
(4, 2)O(7)	1.756	16649.5	1.3	1.5	2.8
(4, 2)S(4)	1.242	17190.4	3.3	4.3	7.5
(4, 2)Q(6)	1.443	17190.4	1.3	1.7	3.0
(4, 2)S(5)	1.226	17808.8	8.5	13.2	21.7
(4, 2)Q(7)	1.459	17808.8	3.2	5.0	8.1
(4, 2)O(9)	1.914	17808.8	0.4	0.7	1.1
(4, 2)S(6)	1.214	18499.1	2.2	4.2	6.5
(4, 2)Q(8)	1.478	18499.1	0.8	1.5	2.3
(4, 2)S(7)	1.205	19256.4	4.9	11.4	16.2
(4, 2)Q(9)	1.499	19256.4	1.8	4.1	5.9
(4, 2)S(8)	1.199	20074.5	1.1	3.2	4.3
(4, 2)Q(10)	1.523	20074.5	0.4	1.2	1.6
(4, 2)S(9)	1.196	20947.5	2.0	7.6	9.6
(4, 2)Q(11)	1.549	20947.5	0.8	3.0	3.9
(4, 2)S(10)	1.196	21869.5	0.4	1.9	2.3
(4, 2)Q(12)	1.579	21869.5	0.2	0.8	1.0
(4, 2)S(11)	1.199	22834.6	0.6	3.9	4.5
(4, 2)Q(13)	1.612	22834.6	0.3	2.0	2.3
(4, 2)S(13)	1.214	24870.3	0.1	1.5	1.6
(4, 2)Q(15)	1.689	24870.3	0.1	1.2	1.3

Table 3. continued.

Line	Wavelength (μm)	$E_{\rm up}$ (cm^{-1})	$F_{2750\ \rm K}$ (10^{-19} W m^{-2})	$F_{6000\ \rm K}$ (10^{-19} W m^{-2})	$F_{\rm tot}$ (10^{-19} W m^{-2})
(4, 3)Q(1)	2.888	15345.8	1.5	1.1	2.6
(4, 3)O(3)	3.376	15345.8	1.3	1.0	2.3
(4, 3)S(1)	2.541	15818.3	2.2	1.9	4.1
(4, 3)Q(3)	2.912	15818.3	1.7	1.5	3.2
(4, 3)O(5)	3.917	15818.3	1.0	0.9	2.0
(4, 3)S(2)	2.435	16190.7	0.8	0.8	1.7
(4, 3)Q(4)	2.931	16190.7	0.6	0.6	1.1
(4, 3)S(3)	2.344	16649.5	2.4	2.7	5.2
(4, 3)Q(5)	2.955	16649.5	1.5	1.7	3.2
(4, 3)S(4)	2.267	17190.4	0.7	0.9	1.5
(4, 3)S(5)	2.201	17808.8	1.4	2.1	3.5
(4, 3)Q(7)	3.018	17808.8	1.0	1.5	2.5
(4, 3)S(7)	2.100	19256.4	0.4	0.8	1.2
(4, 3)Q(9)	3.103	19256.4	0.5	1.1	1.6
(4, 3)S(15)	2.007	27008.8	0.1	1.4	1.4
(4, 3)S(17)	2.047	29205.3	0.0	1.6	1.6
(4, 3)S(19)	2.116	31417.0	0.0	1.5	1.5
(5, 1)S(5)	0.663	20894.9	0.3	1.0	1.2
(5, 1)S(7)	0.664	22251.2	0.2	1.2	1.4
(5, 1)S(9)	0.670	23831.7	0.1	1.1	1.2
(5, 2)S(1)	0.923	19026.0	0.6	1.4	2.0
(5, 2)Q(3)	0.971	19026.0	0.3	0.7	1.1
(5, 2)S(2)	0.912	19376.0	0.3	0.7	1.0
(5, 2)S(3)	0.902	19807.0	1.1	3.1	4.2
(5, 2)Q(5)	0.985	19807.0	0.3	0.9	1.2
(5, 2)S(4)	0.895	20314.8	0.4	1.3	1.7
(5, 2)S(5)	0.890	20894.9	1.1	4.3	5.4
(5, 2)Q(7)	1.006	20894.9	0.2	0.9	1.2
(5, 2)S(6)	0.886	21542.1	0.3	1.5	1.8
(5, 2)S(7)	0.885	22251.2	0.8	4.4	5.2
(5, 2)S(8)	0.886	23016.2	0.2	1.4	1.6
(5, 2)S(9)	0.889	23831.7	0.4	3.6	4.0
(5, 2)S(10)	0.894	24691.8	0.1	1.0	1.1
(5, 2)S(11)	0.901	25590.2	0.2	2.4	2.5
(5, 2)S(13)	0.922	27479.6	0.1	1.3	1.4
(5, 3)Q(1)	1.493	18581.7	1.0	1.9	2.8
(5, 3)O(3)	1.614	18581.7	0.8	1.6	2.5
(5, 3)Q(2)	1.498	18760.3	0.3	0.7	1.0
(5, 3)S(1)	1.400	19026.0	1.6	3.6	5.2
(5, 3)Q(3)	1.506	19026.0	1.2	2.5	3.7
(5, 3)O(5)	1.736	19026.0	0.7	1.6	2.3
(5, 3)S(2)	1.371	19376.0	0.7	1.7	2.4
(5, 3)Q(4)	1.516	19376.0	0.4	1.0	1.4
(5, 3)S(3)	1.347	19807.0	2.3	6.3	8.6
(5, 3)Q(5)	1.529	19807.0	1.1	3.1	4.2
(5, 3)O(7)	1.883	19807.0	0.4	1.0	1.4
(5, 3)S(4)	1.327	20314.8	0.7	2.3	3.1
(5, 3)Q(6)	1.544	20314.8	0.3	1.0	1.4
(5, 3)S(5)	1.311	20894.9	1.9	7.1	9.0
(5, 3)Q(7)	1.563	20894.9	0.8	3.0	3.8
(5, 3)S(6)	1.298	21542.1	0.5	2.2	2.7
(5, 3)Q(8)	1.584	21542.1	0.2	0.9	1.1
(5, 3)S(7)	1.289	22251.2	1.1	5.9	7.0
(5, 3)Q(9)	1.608	22251.2	0.5	2.5	3.0
(5, 3)S(8)	1.284	23016.2	0.2	1.6	1.9
(5, 3)S(9)	1.282	23831.7	0.4	3.7	4.2
(5, 3)Q(11)	1.667	23831.7	0.2	1.9	2.1
(5, 3)S(11)	1.289	25590.2	0.1	1.7	1.9
(5, 3)Q(13)	1.741	25590.2	0.1	1.2	1.3
(5, 4)S(3)	2.507	19807.0	0.3	0.8	1.1
(5, 4)S(17)	2.243	31466.5	0.0	1.0	1.0
(6, 2)S(5)	0.709	23751.0	0.1	1.1	1.2
(6, 2)S(7)	0.711	25013.7	0.1	1.2	1.3
(6, 2)S(9)	0.720	26480.6	0.1	1.1	1.2

Table 3. continued.

Line	Wavelength (μm)	E_{up} (cm^{-1})	$F_{2750\ \mathrm{K}}$ (10^{-19} W m^{-2})	$F_{6000\ \mathrm{K}}$ (10^{-19} W m^{-2})	F_{tot} (10^{-19} W m^{-2})
(6, 3)S(1)	0.988	22005.6	0.2	1.1	1.3
(6, 3)S(3)	0.966	22735.6	0.4	2.3	2.6
(6, 3)S(4)	0.959	23209.8	0.1	0.9	1.0
(6, 3)S(5)	0.954	23751.0	0.4	3.1	3.4
(6, 3)S(6)	0.951	24353.9	0.1	1.1	1.2
(6, 3)S(7)	0.951	25013.7	0.3	3.1	3.4
(6, 3)S(8)	0.953	25724.3	0.1	0.9	1.0
(6, 3)S(9)	0.957	26480.6	0.1	2.5	2.6
(6, 3)S(11)	0.974	28105.8	0.1	1.6	1.6
(6, 4)Q(1)	1.602	21589.8	0.2	1.0	1.2
(6, 4)O(3)	1.733	21589.8	0.2	0.9	1.1
(6, 4)S(1)	1.502	22005.6	0.4	1.9	2.2
(6, 4)Q(3)	1.616	22005.6	0.3	1.4	1.7
(6, 4)O(5)	1.867	22005.6	0.2	0.9	1.1
(6, 4)S(2)	1.471	22332.8	0.2	0.9	1.0
(6, 4)S(3)	1.446	22735.6	0.5	3.2	3.7
(6, 4)Q(5)	1.643	22735.6	0.3	1.7	1.9
(6, 4)S(4)	1.425	23209.8	0.2	1.2	1.3
(6, 4)S(5)	1.408	23751.0	0.4	3.5	3.9
(6, 4)Q(7)	1.683	23751.0	0.2	1.6	1.8
(6, 4)S(6)	1.396	24353.9	0.1	1.1	1.2
(6, 4)S(7)	1.388	25013.7	0.2	2.7	3.0
(6, 4)Q(9)	1.737	25013.7	0.1	1.4	1.5
(6, 4)S(9)	1.384	26480.6	0.1	1.6	1.7
(6, 4)Q(11)	1.807	26480.6	0.1	1.0	1.1
(7, 3)S(7)	0.767	27536.0	0.0	1.1	1.1
(7, 3)S(9)	0.778	28884.1	0.0	1.0	1.0
(7, 4)S(3)	1.040	25430.1	0.1	1.5	1.6
(7, 4)S(5)	1.029	26370.4	0.1	2.0	2.1
(7, 4)S(7)	1.028	27536.0	0.1	1.9	2.0
(7, 4)S(9)	1.039	28884.1	0.0	1.5	1.5
(7, 5)S(3)	1.562	25430.1	0.1	1.5	1.6
(7, 5)S(5)	1.524	26370.4	0.1	1.5	1.6
(7, 5)S(7)	1.506	27536.0	0.0	1.1	1.2
(8, 5)S(5)	1.119	28743.1	0.0	1.2	1.2
(8, 5)S(7)	1.122	29806.1	0.0	1.1	1.1

Table 4. Theoretical H_2 line fluxes, with modeled fluxes between $(0.5-1) \times 10^{-19}$ W m^{-2}.

Line	Wavelength (μm)	E_{up} (cm^{-1})	$F_{2750\ K}$ (10^{-19} W m^{-2})	$F_{6000\ K}$ (10^{-19} W m^{-2})	F_{tot} (10^{-19} W m^{-2})
(0, 0)S(1)	17.035	705.5	0.9	0.0	0.9
(1, 0)O(12)	6.308	9883.8	0.5	0.1	0.6
(1, 0)O(13)	7.126	10927.1	0.5	0.1	0.7
(1, 0)S(12)	1.639	14399.1	0.4	0.2	0.6
(1, 0)Q(16)	2.891	16936.2	0.4	0.5	1.0
(1, 0)S(16)	1.634	19595.7	0.2	0.5	0.7
(1, 0)Q(19)	3.118	20957.7	0.1	0.5	0.6
(1, 0)S(18)	1.659	22333.8	0.1	0.8	1.0
(1, 0)S(20)	1.695	25111.6	0.1	0.9	0.9
(2, 0)O(11)	1.834	12584.8	0.5	0.2	0.6
(2, 0)Q(16)	1.496	20161.8	0.1	0.4	0.5
(2, 0)Q(19)	1.616	23939.6	0.1	0.5	0.5
(2, 1)O(10)	5.410	11732.1	0.8	0.2	1.0
(2, 1)S(11)	1.753	16632.1	0.4	0.4	0.8
(2, 1)Q(17)	3.177	21400.9	0.1	0.6	0.8
(2, 1)S(16)	1.747	22661.7	0.1	0.7	0.8
(2, 1)S(18)	1.775	25228.7	0.1	0.9	1.0
(2, 1)S(20)	1.822	27823.0	0.0	0.9	0.9
(2, 2)S(20)	3.855	27823.0	0.0	0.8	0.9
(3, 0)O(3)	0.895	11883.5	0.5	0.2	0.7
(3, 0)S(0)	0.827	12084.7	0.5	0.2	0.7
(3, 0)Q(2)	0.852	12084.7	0.4	0.1	0.6
(3, 0)Q(4)	0.861	12778.8	0.5	0.2	0.7
(3, 0)Q(6)	0.875	13839.2	0.4	0.2	0.6
(3, 0)Q(11)	0.934	17833.8	0.3	0.4	0.7
(3, 0)S(12)	0.792	20918.2	0.2	0.6	0.7
(3, 0)S(15)	0.820	24321.2	0.1	0.6	0.7
(3, 1)O(11)	1.958	16033.8	0.3	0.3	0.5
(3, 1)Q(14)	1.534	20918.2	0.2	0.7	0.9
(3, 1)S(14)	1.141	23161.0	0.1	0.6	0.7
(3, 1)S(15)	1.153	24321.2	0.1	0.9	1.0
(3, 1)Q(19)	1.744	26691.8	0.0	0.5	0.5
(3, 2)O(8)	4.746	13839.2	0.5	0.3	0.8
(3, 2)Q(12)	3.049	18816.8	0.2	0.5	0.7
(3, 2)S(13)	1.854	22025.0	0.1	0.6	0.8
(3, 2)Q(15)	3.252	22025.0	0.1	0.6	0.7
(3, 2)S(16)	1.873	25499.7	0.0	0.7	0.7
(3, 2)S(18)	1.912	27891.6	0.0	0.8	0.8
(3, 2)S(20)	1.973	30296.3	0.0	0.7	0.7
(3, 3)S(8)	5.970	16904.0	0.3	0.3	0.6
(3, 3)S(10)	5.228	18816.8	0.3	0.5	0.8
(3, 3)S(12)	4.759	20918.2	0.2	0.7	0.9
(3, 3)S(14)	4.459	23161.0	0.1	0.7	0.8
(3, 3)S(16)	4.276	25499.7	0.0	0.6	0.6
(4, 0)S(3)	0.627	16649.5	0.3	0.3	0.6
(4, 0)S(5)	0.622	17808.8	0.4	0.6	0.9
(4, 0)S(7)	0.622	19256.4	0.3	0.7	1.0
(4, 0)S(9)	0.627	20947.5	0.2	0.6	0.8
(4, 0)S(11)	0.637	22834.6	0.1	0.5	0.6
(4, 1)O(3)	0.951	15345.8	0.3	0.3	0.6
(4, 1)S(0)	0.879	15535.7	0.3	0.2	0.5
(4, 1)Q(4)	0.916	16190.7	0.3	0.3	0.6
(4, 1)Q(6)	0.931	17190.4	0.2	0.3	0.6
(4, 1)Q(11)	0.998	20947.5	0.2	0.7	0.8
(4, 1)Q(13)	1.037	22834.6	0.1	0.5	0.5
(4, 1)S(12)	0.847	23836.6	0.1	0.7	0.8
(4, 1)S(15)	0.880	27008.8	0.0	0.8	0.8

Table 4. continued.

Line	Wavelength (μm)	$E_{\rm up}$ (cm^{-1})	$F_{2750\ \rm K}$ (10^{-19} W m^{-2})	$F_{6000\ \rm K}$ (10^{-19} W m^{-2})	$F_{\rm tot}$ (10^{-19} W m^{-2})
(4, 2)O(8)	1.832	17190.4	0.3	0.3	0.6
(4, 2)S(12)	1.205	23836.6	0.1	0.8	0.9
(4, 2)Q(14)	1.649	23836.6	0.1	0.5	0.6
(4, 2)Q(17)	1.783	27008.8	0.0	0.7	0.7
(4, 3)O(2)	3.159	15250.3	0.3	0.2	0.6
(4, 3)S(0)	2.664	15535.7	0.4	0.4	0.8
(4, 3)Q(2)	2.898	15535.7	0.5	0.4	0.9
(4, 3)O(4)	3.627	15535.7	0.4	0.4	0.8
(4, 3)O(7)	4.642	16649.5	0.5	0.5	1.0
(4, 3)Q(6)	2.984	17190.4	0.4	0.5	1.0
(4, 3)S(6)	2.146	18499.1	0.3	0.5	0.8
(4, 3)Q(8)	3.058	18499.1	0.2	0.4	0.7
(4, 3)Q(11)	3.212	20947.5	0.2	0.7	0.9
(4, 3)S(13)	1.991	24870.3	0.1	0.8	0.8
(4, 3)S(16)	2.024	28102.3	0.0	0.5	0.5
(4, 3)S(18)	2.078	30311.8	0.0	0.5	0.5
(4, 4)S(9)	5.913	20947.5	0.1	0.4	0.6
(4, 4)S(11)	5.299	22834.6	0.1	0.7	0.8
(4, 4)S(13)	4.912	24870.3	0.1	0.8	0.8
(4, 4)S(15)	4.676	27008.8	0.0	0.7	0.7
(4, 4)S(17)	4.553	29205.3	0.0	0.5	0.6
(5, 1)S(3)	0.668	19807.0	0.2	0.6	0.8
(5, 1)S(11)	0.682	25590.2	0.1	0.8	0.9
(5, 1)S(13)	0.700	27479.6	0.0	0.5	0.6
(5, 2)Q(1)	0.963	18581.7	0.3	0.5	0.8
(5, 2)Q(9)	1.035	22251.2	0.2	0.8	1.0
(5, 2)Q(11)	1.071	23831.7	0.1	0.7	0.7
(5, 2)Q(13)	1.116	25590.2	0.0	0.5	0.5
(5, 2)S(12)	0.910	26521.4	0.0	0.6	0.6
(5, 2)S(15)	0.952	29453.8	0.0	0.6	0.6
(5, 3)O(2)	1.561	18491.9	0.2	0.4	0.6
(5, 3)S(0)	1.433	18760.3	0.3	0.6	0.9
(5, 3)O(4)	1.672	18760.3	0.3	0.6	0.9
(5, 3)O(6)	1.806	19376.0	0.2	0.4	0.6
(5, 3)O(9)	2.057	20894.9	0.1	0.5	0.7
(5, 3)Q(10)	1.636	23016.2	0.1	0.7	0.8
(5, 3)S(10)	1.284	24691.8	0.1	0.9	1.0
(5, 3)Q(12)	1.702	24691.8	0.0	0.5	0.6
(5, 3)S(13)	1.310	27479.6	0.0	0.5	0.5
(5, 3)Q(15)	1.833	27479.6	0.0	0.8	0.8
(5, 4)Q(1)	3.090	18581.7	0.2	0.4	0.6
(5, 4)O(3)	3.619	18581.7	0.2	0.4	0.6
(5, 4)S(1)	2.717	19026.0	0.3	0.6	0.9
(5, 4)Q(3)	3.117	19026.0	0.2	0.5	0.8
(5, 4)Q(5)	3.167	19807.0	0.2	0.6	0.8
(5, 4)S(5)	2.355	20894.9	0.1	0.5	0.7
(5, 4)Q(7)	3.240	20894.9	0.1	0.5	0.7
(5, 4)S(13)	2.153	27479.6	0.0	0.7	0.7
(5, 4)S(15)	2.182	29453.8	0.0	1.0	1.0
(5, 4)S(19)	2.344	33471.2	0.0	0.9	0.9
(6, 2)S(3)	0.714	22735.6	0.1	0.7	0.8
(6, 2)S(11)	0.735	28105.8	0.0	0.9	0.9
(6, 2)S(13)	0.757	29841.8	0.0	0.6	0.6
(6, 3)Q(1)	1.030	21589.8	0.1	0.4	0.5
(6, 3)Q(3)	1.039	22005.6	0.1	0.6	0.7
(6, 3)S(2)	0.976	22332.8	0.1	0.6	0.7
(6, 3)Q(5)	1.056	22735.6	0.1	0.7	0.9
(6, 3)Q(7)	1.080	23751.0	0.1	0.8	0.9

Table 4. continued.

Line	Wavelength (μm)	E_{up} (cm^{-1})	$F_{2750\ K}$ (10^{-19} W m^{-2})	$F_{6000\ K}$ (10^{-19} W m^{-2})	F_{tot} (10^{-19} W m^{-2})
(6, 3)Q(9)	1.114	25013.7	0.1	0.7	0.8
(6, 3)Q(11)	1.157	26480.6	0.0	0.6	0.6
(6, 3)S(10)	0.964	27276.4	0.0	0.7	0.7
(6, 3)S(13)	1.001	29841.8	0.0	0.8	0.8
(6, 4)Q(4)	1.628	22332.8	0.1	0.5	0.6
(6, 4)O(7)	2.030	22735.6	0.1	0.6	0.7
(6, 4)Q(6)	1.661	23209.8	0.1	0.6	0.6
(6, 4)Q(8)	1.708	24353.9	0.1	0.5	0.6
(6, 4)S(8)	1.384	25724.3	0.0	0.7	0.8
(6, 4)S(11)	1.397	28105.8	0.0	0.6	0.6
(6, 4)Q(13)	1.897	28105.8	0.0	0.7	0.7
(6, 5)S(13)	2.352	29841.8	0.0	0.5	0.5
(6, 5)S(15)	2.403	31641.1	0.0	0.6	0.6
(6, 5)S(17)	2.500	33453.8	0.0	0.6	0.6
(7, 3)S(3)	0.767	25430.1	0.0	0.6	0.6
(7, 3)S(5)	0.763	26370.4	0.1	0.9	1.0
(7, 3)S(11)	0.798	30368.2	0.0	0.7	0.7
(7, 4)S(1)	1.063	24752.5	0.1	0.7	0.8
(7, 4)Q(5)	1.139	25430.1	0.0	0.6	0.6
(7, 4)S(4)	1.033	25869.5	0.0	0.6	0.6
(7, 4)Q(7)	1.168	26370.4	0.0	0.6	0.6
(7, 4)S(6)	1.027	26927.7	0.0	0.7	0.7
(7, 4)Q(9)	1.208	27536.0	0.0	0.5	0.6
(7, 4)S(8)	1.032	28190.1	0.0	0.6	0.6
(7, 4)S(11)	1.061	30368.2	0.0	0.9	0.9
(7, 5)Q(1)	1.729	24366.1	0.1	0.5	0.6
(7, 5)O(3)	1.873	24366.1	0.1	0.5	0.6
(7, 5)S(1)	1.621	24752.5	0.1	0.9	1.0
(7, 5)Q(3)	1.746	24752.5	0.1	0.7	0.8
(7, 5)O(5)	2.022	24752.5	0.0	0.5	0.6
(7, 5)Q(5)	1.778	25430.1	0.1	0.9	0.9
(7, 5)S(4)	1.540	25869.5	0.0	0.5	0.6
(7, 5)Q(7)	1.826	26370.4	0.0	0.8	0.9
(7, 5)Q(9)	1.892	27536.0	0.0	0.7	0.7
(7, 5)S(9)	1.508	28884.1	0.0	0.5	0.6
(7, 5)Q(11)	1.979	28884.1	0.0	0.5	0.5
(8, 4)S(3)	0.829	27881.7	0.0	0.5	0.5
(8, 4)S(5)	0.827	28743.1	0.0	0.7	0.8
(8, 4)S(7)	0.834	29806.1	0.0	0.8	0.8
(8, 4)S(9)	0.850	31027.0	0.0	0.7	0.7
(8, 4)S(11)	0.876	32358.5	0.0	0.5	0.5
(8, 5)S(3)	1.129	27881.7	0.0	0.9	1.0
(8, 5)S(9)	1.139	31027.0	0.0	0.8	0.8
(8, 6)S(3)	1.702	27881.7	0.0	0.6	0.7
(8, 6)S(5)	1.665	28743.1	0.0	0.6	0.6
(9, 5)S(5)	0.905	30854.1	0.0	0.5	0.5
(9, 5)S(7)	0.917	31805.9	0.0	0.6	0.6
(9, 6)S(3)	1.239	30077.2	0.0	0.6	0.6
(9, 6)S(5)	1.232	30854.1	0.0	0.7	0.7
(9, 6)S(7)	1.241	31805.9	0.0	0.6	0.6

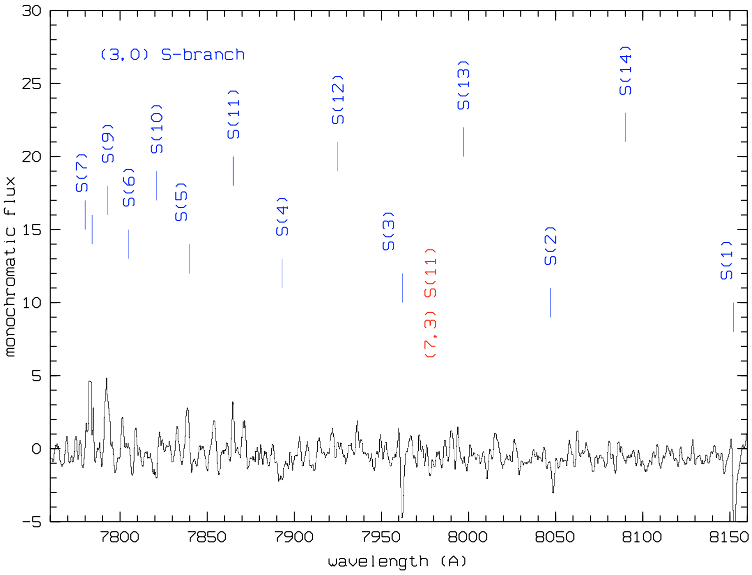

Fig. 10. Residuals between observed and modeled H_2 spectra as shown in Fig. 1, covering the range of 7760–8160 Å. The expected positions of the (3, 0) S(1)–S(14) lines are indicated.

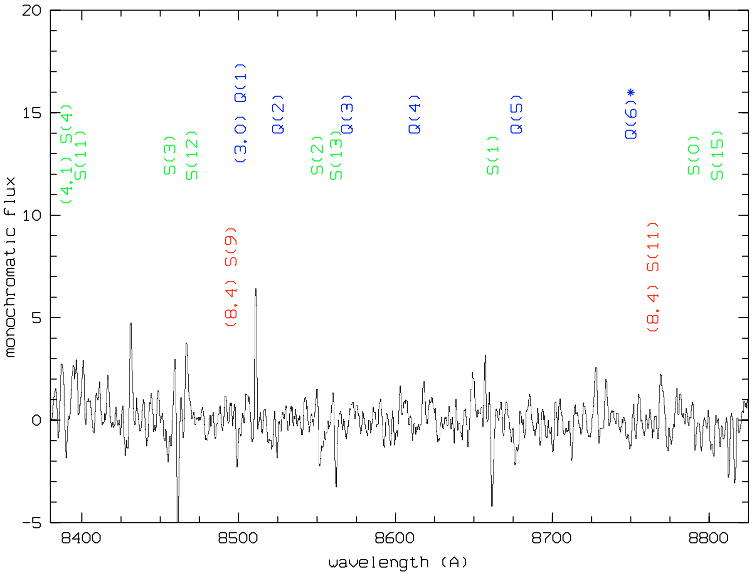

Fig. 11. Residuals between observed and modeled H_2 spectra as shown in Fig. 2, covering the range of 8390–8820 Å. The expected positions of various emission lines in the (3, 0) and (4, 1) bands are indicated. The feature near 8510 Å is a spike and does not correspond to an H_2 emission line.

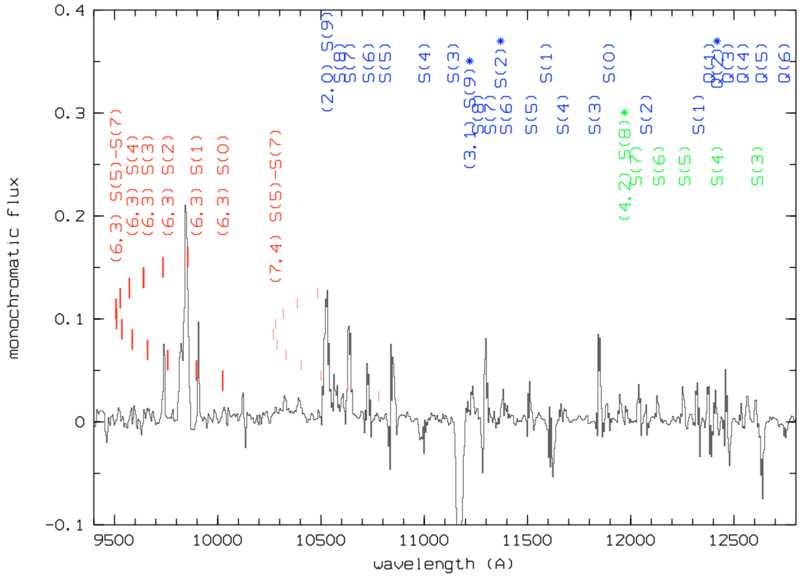

Fig. 12. Residuals between observed and modeled H_2 spectra as shown in Fig. 3, covering the range of 9400–12 800 Å. The modeled flux in the (3, 1) S(9), S(10), S(11) blend near 11 200 Å is too high by a factor of about 2.

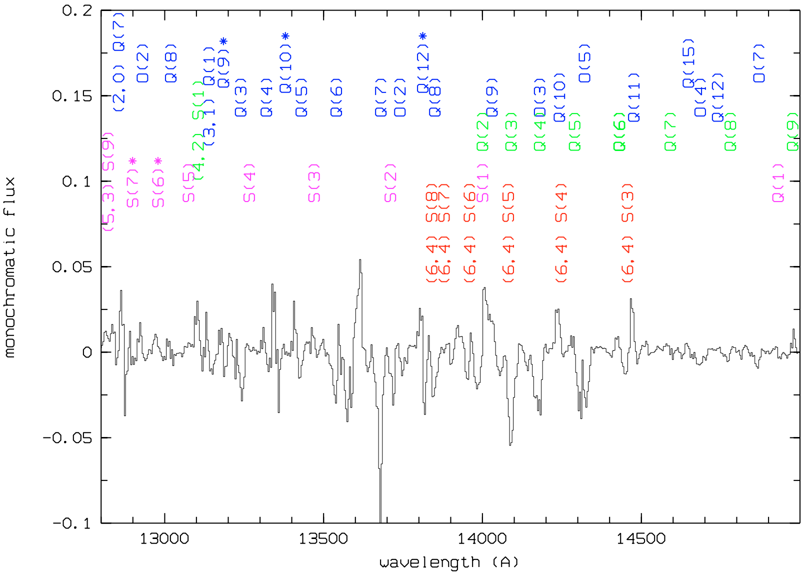

Fig. 13. Residuals between observed and modeled H_2 spectra as shown in Fig. 4, covering the range of 12 800–15 000 Å. The modeled flux in the (3, 1) Q(7) line is too high by a factor of about 2. The spectral region between 13 500–14 500 Å is characterized by poor atmospheric transmission.

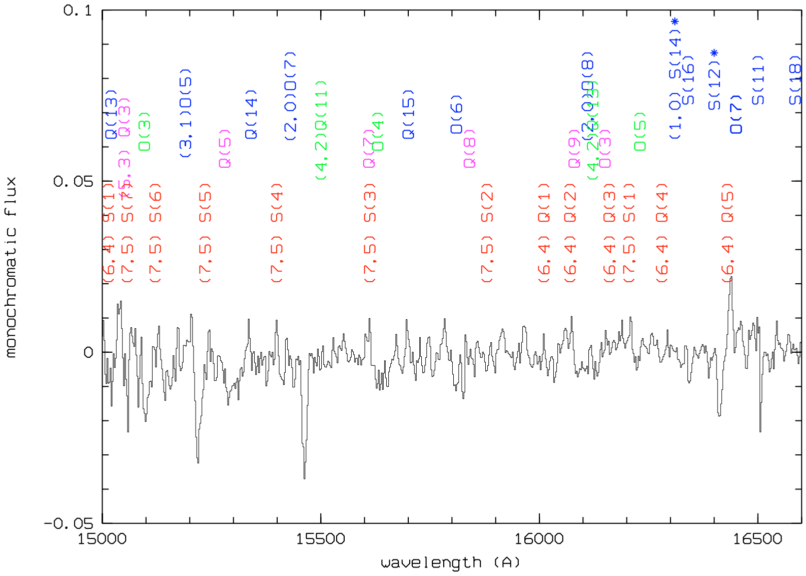

Fig. 14. Residuals between observed and modeled H_2 spectra as shown in Fig. 5, covering the range of 15 000–16 600 Å. The flux in the (3, 1) O(5) and (2, 0) O(7) lines is too strong by a factor of about 2.

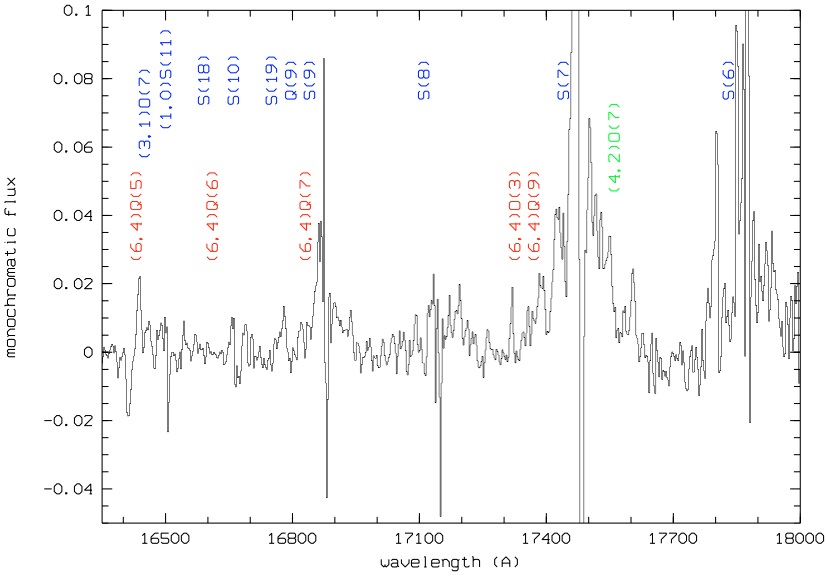

Fig. 15. Residuals between observed and modeled H_2 spectra as shown in Fig. 6, covering the range of 16 350–18 000 Å. The line wings in the (1, 0) S(7) and S(8) lines arise from an instrumental defect of SOFI and have no astrophysical significance.

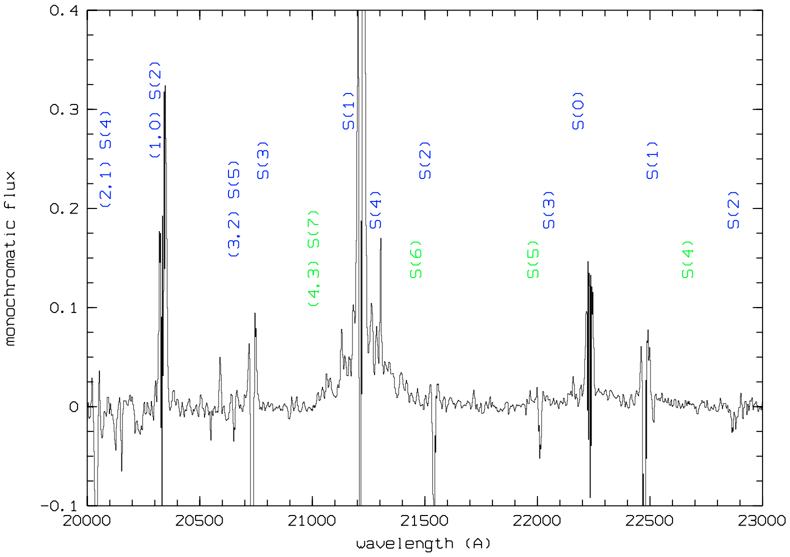

Fig. 16. Residuals between observed and modeled H_2 spectra as shown in Fig. 7, covering the range of 20 000–23 000 Å. The broad line wings in the (1, 0) S(1) line arise from an instrumental defect of SOFI.